Automated Homogenization-Based Fracture Analysis: Effects of SVE Size and Boundary Condition

Bahador Bahmani[a], Ming Yang[b], Anand Nagarajan[b], Philip L Clarke[a], Soheil Soghrati[b,c], Reza Abedi[a,*]

[a] *Dept. of Mechanical, Aerospace and Biomedical Engineering, The University of Tennessee, Space Institute, TN, USA*
[b] *Dept. of Mechanical and Aerospace Engineering, The Ohio State University, OH, USA*
[c] *Dept. of Materials Science and Engineering, The Ohio State University, OH, USA*

Abstract

To model the sample-to-sample variations and the effect of microscale inhomogeneities on fracture response, statistical volume elements (SVEs) are employed to homogenize the elastic and fracture properties of ZrB_2-SiC, a two-phase particulate composite often used as a thermal coating. In the mesoscale analysis, 2D finite element models are generated using a non-iterative, automated mesh generation algorithm named Conforming to Interface Structured Adaptive Mesh Refinement (CISAMR). The analysis of SVEs under mixed, traction, and minimal kinematic boundary conditions yields their angle-dependent tensile and shear fracture strengths and elastic stiffnesses. This study shows that homogenized fracture strengths are highly dependent on the SVE size and the particular geometric distribution of inclusions (even for similar volume ratios), whereas elastic properties are mainly a function of the volume fraction. Moreover, mean values of strength and bulk modulus, respectively, decrease and remain almost constant as the SVE size increases. For the macroscale analysis, an isotropic, inhomogeneous field of fracture strength is generated from the homogenization of SVEs. The asynchronous Spacetime Discontinuous Galerkin (aSDG) method is subse-

*Corresponding author: Associate professor of Mechanical Aerospace and Biomedical Engineering, University of Tennessee, 411 B.H. Goethert Parkway, Tullahoma, TN, 37388, USA.

Email address: rabedi@utk.edu (Reza Abedi)

quently employed for fracture analysis under uniaxial tensile and thermal strain loadings.

Keywords: Statistical volume element, Brittle fracture, Size effect, Mesh generation, CISAMR, Spacetime Discontinuous Galerkin

1. Introduction

Unlike the elastic response, fracture and damage are inherently local phenomena, in that they often initiate from microstructural defects or material interfaces. For ductile materials, diffused areas undergoing large plastic deformation reduce their sensitivity to microstructural design. On the other hand, due to the lack of significant bulk energy dissipative mechanisms, quasi-brittle materials are highly sensitive to their microstructure [1, 2]. Some consequence of the (high) dependency of the failure response on microstructural design are localized zones of failure even in the absence of macroscopic stress concentration points [3], variations of the fracture pattern under the same problem set-up [4], ultimate strength/fracture energy uncertainties [5, 6], and decrease of the mean and the variation of fracture strength known as the *size effect* [7].

Material defects and other microstructural features can be modeled either explicitly or implicitly [8]. *Explicit* models directly incorporate defects larger than a certain size in the analysis. However, due to the high computational cost, their use is limited to small space and time scales. *Implicit* approaches, on the other hand, only represent the impact of defects in an averaged, statistical, or homogenized sense. For example, the Weibull's weakest link model [9, 10] can qualitatively explain the size effect. Also, Abedi *et al.* showed that by assigning point-wise values of fracture strength based on the Weibull model, realistic fracture patterns can be captured for problems that lack macroscopic stress concentration points, *e.g.,* fracture under dynamic compressive loading [11] and fragmentation [12] studies. However, many of such phenomenological models lack a direct connection to the material microstructure. As will be discussed next, homogenization approaches address this concern and provide a direct link between micro and macro scales by *averaging* the response in a Volume Element.

Continuum thermomechanics is founded on the concept of *Representative Volume Element* (RVE), which is well defined for [13]: (i) a unit cell in a periodic microstructure; and (ii) a statistically representative *Volume*

Element (VE) containing a large number of microscale elements. There are many popular criteria to decide whether a VE is large enough to be considered representative for group (ii); see for example [14, 15] and the references therein. Under such conditions, the material in an RVE can be represented as a continuum. Several classical homogenization approaches attempt to obtain effective material properties of an RVE; *cf.* [16, 17, 18, 19, 20, 21].

An RVE is not well-defined, when neither of the two aforementioned conditions is satisfied. Then, the so-called *Statistical Volume Element* (SVE) may still represent the material in continuum form, although the randomness in material properties must be properly characterized. Perturbations to geometry and material properties of a periodic unit cell violate the definition of group (i) RVEs and are the basis for the definition of SVEs in [22, 23, 24, 25]. When a VE is not large enough to be considered an RVE from group (ii), a collection of them should be considered to characterize the statistics of the homogenized property. For these SVEs, the type of boundary conditions [26], clustering/positioning of microstructures [27], and variations in the observation window [28, 29] all affect the statistics of the homogenized properties.

Beyond numerous works in the elastic regime, RVEs are used in [30, 31, 32, 33, 34] to homogenize and calibrate various fracture models. Yet, the statistical characterization of fracture properties of a material by SVEs can be more advantageous; first, by maintaining some level of heterogeneity, even for a macroscopically homogeneous material, weak points of a realization based on SVE statistics can result in localized fracture for problems that lack macroscopic stress concentration points. Second, variations in the fracture pattern, ultimate load, and fracture energy all can be represented by realizing random fields that are consistent with the statistics of values homogenized by SVEs. Thus, by differing from RVEs in preserving the spatial and sample-to-sample variations, they address several concerns of a macroscopic model for failure analysis. Yet, the analysis of domains characterized by SVEs can be significantly more economical than an explicit approach, as microstructural features are no longer directly incorporated in the (computational) model.

The goal of the this manuscript is to use SVEs to homogenize both elastic and fracture properties and subsequently employ the homogenized fields for macroscopic dynamic fracture analysis. The material system adopted for this study is a ZrB_2-SiC particulate composite, which is often implemented as a thermal barrier coating for ultra-high temperature applications. While the ZrB_2 matrix has a high melting point and thermal stability, embedded

SiC particles improve the oxidation resistance of the resulting composite material in aggressive environments. A new microstructure reconstruction algorithm relying on animation-inspired packing and optimization phases [35, 36] is employed to virtually build a realistic RVE of this ZrB_2-SiC based on morphological and statistical information extracted from imaging data. Thousands of SVEs with different sizes are then extracted from this RVE to simulate their micromechanical behavior subject to macroscopic tensile and shear loads. In order to automate the modeling process, a new mesh generation algorithm, named Conforming to Interface Structure Adaptive Mesh Refinement (CISAMR) [37, 38, 39] is implemented to build the finite element (FE) model associated with each SVE. The unique feature of CISAMR is the ability to non-iteratively transform a simple structured grid into a high-quality conforming mesh for problems with complex morphologies.

Although SVEs have been used for fracture analysis studies (*e.g.,* [40, 41]), these SVEs were not constructed based on realistic material microstructures; *i.e.,* limited to domains containing micro-cracks [40] and circular inclusions [41]. Further, highly simplified models were used to derive fracture initiation strengths, in that micro-cracks did not interact [40] and fracture could only nucleate at interfaces between matrix and inclusion phases [42]. One of the main contributions of this manuscript is providing a significantly more accurate characterization and analysis of SVEs compared to [40, 42]. The virtual microstructure reconstruction results in a highly realistic representation of ZrB_2-SiC RVE, together with CISAMR, enables constructing highly-fidelity FE simulations at the SVE level. Beyond these advances in modeling capabilities, the fracture initiation criteria not only takes into account the damage nucleation along particle-matrix interfaces [41] but also allows its initiation in each phase separately.

The second key contribution of this work is the in-depth analysis of homogenized elastic and fracture properties. The homogenization of SVEs is formulated for traction, mixed displacement / traction, and minimal kinematic boundary conditions (BCs). In addition, normal and shear fracture strengths are characterized for arbitrary angle of loading. Several interesting trends are observed by investigating the effect of BCs, SVE size, and other parameters. For example, for the same SVE size and microscopic volume fraction of inclusions, the bulk modulus is rather constant while the fracture strengths are highly variable, implying its sensitivity to the geometric distribution of inclusions in SVE. Moreover, homogenized fracture strength and bulk modulus exhibit different dependencies on the size of SVE. Finally,

the importance and impact of using the SVE-homogenized fracture strength field on macroscopic fracture response is shown through two examples.

The outline of the manuscript is schematically shown in fig. 1. At the macroscale, the algorithm in §2.1 is employed to construct a microscopic realization of the ZrB_2-SiC RVE. This RVE divided into non-overlapping SVEs, entailing meshing by CISAMR, solution, and derivation of elastic and fracture properties of SVEs is entirely discussed in §3. We then implement a *numerical homogenization* approach in that homogenized properties will be used as material properties of RVE; *cf.* third subfigure in fig. 1. The formulation and calibration of an interfacial damage model, based on the homogenized fracture strength field are described in §2.2 and §2.3, respectively. Subsequently, the *asynchronous Spacetime Discontinuous Galerkin* (aSDG) method, *cf.* §2.4, is used for RVE dynamic fracture analysis. The analysis of the statistics of homogenized elastic and fracture properties and two fracture simulations the RVE scale for uniaxial tensile and thermal strain loadings are presented in §4. Final conclusions are drawn in §5.

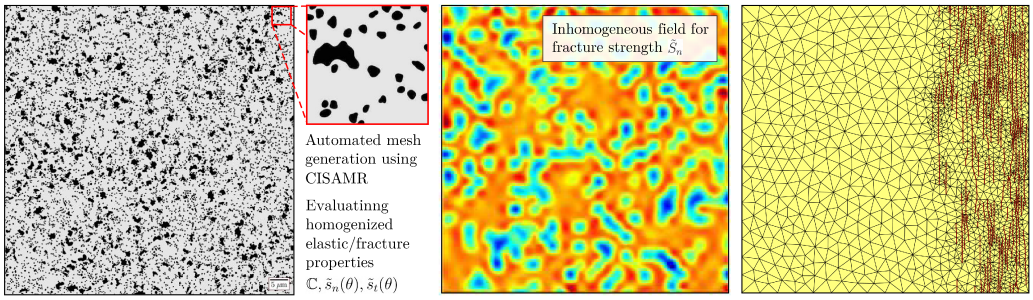

Figure 1: Different modeling steps of the homogenization-based dynamic fracture analysis presented in this manuscript.

2. Macroscopic dynamic fracture analyses

2.1. Virtual microstructure reconstruction

Figure 2a illustrates the $800\,\mu\text{m}\times800\,\mu\text{m}$ RVE of the ZrB_2-SiC composite studied in this manuscript, which is synthesized using a simplified version of the reconstruction algorithm recently introduced in [35]. In this section,

we provide a brief overview of this algorithm, which relies on a hierarchical bounding box (BBox) representation of particles to virtually pack them in the domain. Morphologies of SiC particles in this RVE are extracted from scanning electron microscopy (SEM) images of a ZrB_2-SiC thermal coating presented in [43]. After the segmentation of images to isolate a representative set of inclusions composed of 97 particles, their morphologies are characterized in terms of Non-Uniform Rational Basis Splines (NURBS) [44] and stored in a shape library. NURBS are parametric functions that can accurately describe geometries of randomly-shaped objects and in this work provide an explicit representation of material interfaces in synthesized RVE.

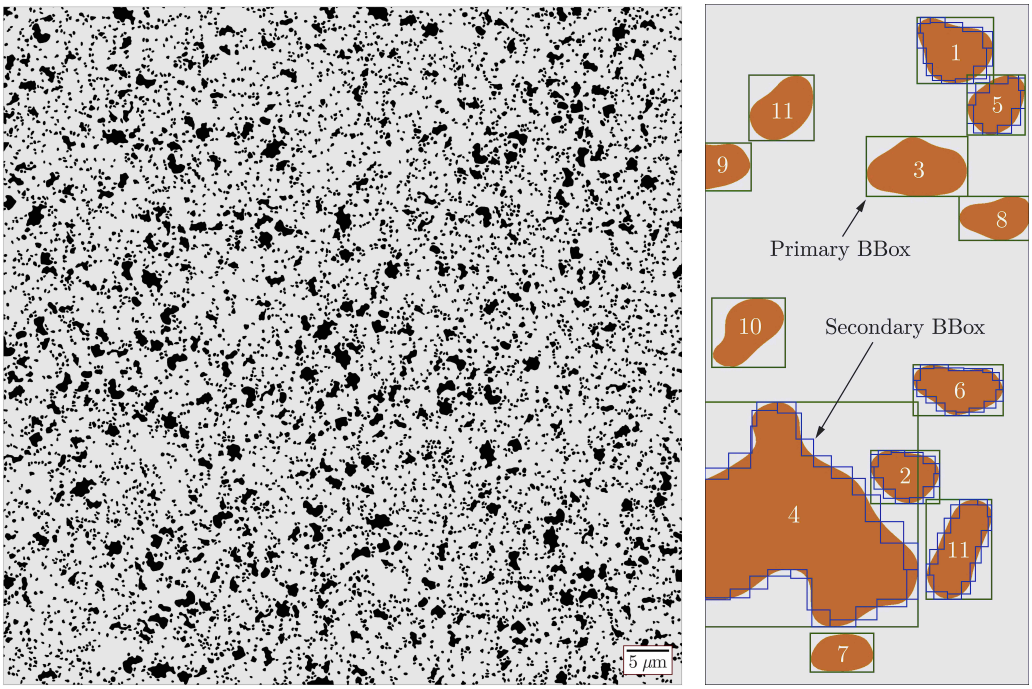

(a) (b)

Figure 2: (a) Virtually reconstructed ZrB_2-SiC RVE with $V_f = 20\%$; (b) checking intersections between hierarchical BBoxes of embedded particles during the packing process.

The virtual reconstruction of the ZrB_2-SiC microstructure involves selecting a particle $\mathcal{P}_i$ from the shape library, rotating that at a random angle $0 < \theta < 2\pi$, and trying to add that to RVE at an arbitrary location $\mathbf{x}_i$. Clearly, $\mathcal{P}_i$ can be embedded in at this location only if it does not overlap

with any of the existing particles. Otherwise, a new random location must be assigned to $\mathcal{P}_i$ and the process is continued until the volume fraction V_f of particles reaches the target value. As shown in fig. 2b, a set of hierarchical (primary and secondary) BBoxes representing each particle is employed to identify overlaps between new and existing particles during the packing process. Note that the secondary BBoxes shown in this figure are defined on a set of consecutive points on the periphery of each particle, coordinates of which are calculated using the NURBS function characterizing its shape.

In order to add a new particle to RVE, we first check intersections between its primary BBox with those of existing particles. If no overlap is detected, this computationally inexpensive calculation (heuristic check) gives the permission to embedded the new particle in RVE at the designated location. In order to further enhance this process, a quadtree search algorithm is employed to quickly identify existing particles in the vicinity of a new particle and minimize the corresponding computational cost. This avoids the unnecessary checking of intersections between primary BBox of a new particle and those of hundreds or thousands of existing particles far away from that. Assuming that the numbering shows in fig. 2b corresponds to the order at which particles are embedded in RVE, this approach would be sufficient to determine that particles 1, 2, 3, 7, 8, 9, 10, and 12 can be added to the microstructure without overlapping with any of previously embedded particles.

Given the arbitrary shape of particles used in the virtual reconstruction of the ZrB_2-SiC microstructure, some of which with concave geometries (*cf.*, fig. 2a), checking intersections between primary BBoxes of new and existing particles overestimates the overlap between them. In other words, it is still probable that two particles do not intersect with one another although their primary BBoxes does, which is the case for particles 1-5, 2-4, 4-6, and 2-11 in fig. 2b. In such cases, we proceed to checking intersections between secondary BBoxes of each pair of particles to more accurately determine whether they overlap with one another or not. To minimize the number of calculations at this stage, we first identify the overlapping box of primary BBoxes of each pair of particles. If none of the secondary BBoxes of the new particle intersects with this box, the particles do not overlap and the new particle can be added to the microstructure (pairs 4-6 and 2-11). Otherwise, the same task is carried out for secondary BBoxes of the existing particle and the overlapping box to determine the feasibility of adding the new particle. If some of the secondary BBoxes of both the new and existing particles intersect with the overlapping region of their primary BBoxes, they still may

not overlap with one another if none of these secondary BBoxes intersect with one another (*cf.*, pairs 1-5 and 2-4).

The BBox-based packing algorithm described above yields a virtual microstructure with a relatively uniform spatial arrangement of particles in the domain. However, this is clearly not the case for the RVE shown in fig. 2b, where particles are locally clustered in some regions and larger particles are non-uniformly distributed within the domain. In order to synthesize this RVE, particles are first packed within the domain at a higher volume fraction than the target value, i.e., with a volume fraction of $V_{\text{raw}} = 45\%$ compared to a target value of $V_f = 20\%$. A multi-objective Genetic Algorithm (GA) [45, 46] is then employed to selectively eliminate some of the particles from the initial (raw) microstructure not only to cut back the volume fraction to $V_f = 20\%$ but also to achieve the desired size distribution and spatial arrangement for them. The latter two statistical microstructural descriptors are characterized using a log-normal distribution function (size distribution) and a two-point correlation function (spatial arrangement). Although the reconstruction algorithm is able to generate high-quality virtual microstructures by using the statistical descriptors directly extracted from SEM images, these descriptors in the current study are artificially designed to achieve a non-homogeneous spatial arrangement of particles with distinct variations in their sizes. This ensures a large variation of homogenized properties (e.g., strength) of SVEs with different sizes at different locations within RVE, which in turn better highlights the effect of the SVE size on resulting *Probability Distribution Functions* (PDFs) and the fracture response. More details regarding the GA-based optimization phase used for the reconstruction of RVE shown in fig. 2b are presented in [35].

2.2. Macroscopic interfacial damage model

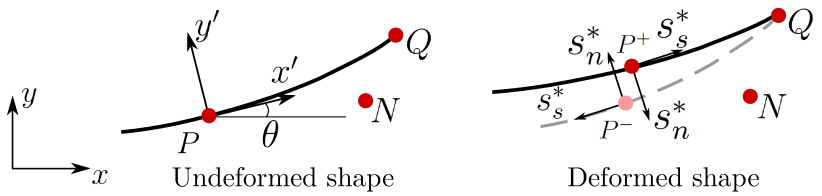

Figure 3: Target traction $\mathbf{s}^* = [s_n^*,\ s_s^*]$ shown in the local coordinate system (x', y') on a fracture surface.

Figure 3 shows the point P on a crack surface. The local coordinate system (x', y') is at angle θ with respect to the global system x, y. Interfacial constitutive equations relate the mechanical fields from the two sides of the interface to the traction target vector $\mathbf{s}^* = [s_n^*,\ s_s^*]$ on P. For example, traditional cohesive models, *e.g.,* [47, 48, 49], employ a *Traction-Separation Relation* (TSR) to related the separation vector $\Delta\mathbf{u} = P^+ - P^-$ to the traction $\mathbf{s}^*$. In lieu of a TSR we employ an interfacial damage model [12]. A damage parameter D linearly interpolates between fully bonded ($D = 0$) and debonded ($D = 1$) states; thus, $\mathbf{s}^*$ is given by,

$$\mathbf{s}^* := (1 - D)\breve{\mathbf{s}}^{\mathrm{B}} + D\breve{\mathbf{s}}^{\mathrm{D}}, \tag{1}$$

where $\breve{\mathbf{s}}^{\mathrm{B}}$ and $\breve{\mathbf{s}}^{\mathrm{D}}$ are dynamic traction solutions for perfectly bonded and debonded interfaces obtained by a local Riemann solution [50]. A similar equation interpolates target velocity values for each side of the interface.

At point P, $\breve{s}_n^{\mathrm{B}}(\theta)$ and $\breve{s}_s^{\mathrm{B}}(\theta)$ denote the normal and shear components of bonded traction $\breve{\mathbf{s}}^{\mathrm{B}}$, along x' and y' directions, respectively. The *effective stress*, defined by

$$\breve{s}(\theta) := \sqrt{\langle \breve{s}_n^{\mathrm{B}}(\theta)\rangle^2 + \left(\beta(\theta)\breve{s}_s^{\mathrm{B}}(\theta)\right)^2}, \tag{2}$$

drives the damage evolution. The positive part operator $\langle . \rangle$ ensures that compressive normal traction does not contribute to damage evolution, and $\beta(\theta)$ is the macroscopic mode mixity at angle θ [12]. A time-delay model similar in form to that in [51, 52] is used to govern the damage evolution,

$$\dot{D} = \frac{1}{\tilde{\tau}} G(\langle D_t - D\rangle) \tag{3}$$

where D_t is the damage value that would have been realized under quasi-static conditions and G is a monotonically increasing function satisfying $D(0) = 0$ and $G(\langle D_t - D\rangle) \leq 1$. The form of (3) implies that $0 \leq \dot{D} \leq 1/\tilde{\tau}$ and $\dot{D} \to 0$ when $D \to D_t$. Damage evolution is *stress-driven* in that D_t is a function of the ratio of $\breve{s}(\theta)$ to *quasi-static tensile strength* $\tilde{s}_n(\theta)$ at angle θ. Thus, (2) implies that mode mixity is given by,

$$\beta(\theta) := \frac{\tilde{s}_n(\theta)}{\tilde{s}_s(\theta)}. \tag{4}$$

where $\tilde{s}_s(\theta)$ is the *quasi-static shear strength* at angle θ.

2.3. SVE-homogenized properties for macroscopic fracture analysis

The fracture response of quasi-brittle materials is highly sensitive to their microstructure. Specially in fragmentation, due to the lack of macroscopic stress concentration points, inhomogeneity of material properties greatly affects the fracture response. For example, it has been shown in [3] that unrealistic patterns are observed when homogeneous fields are used for elastic and fracture properties. In contrast, if inhomogeneities are resolved at a sufficiently small scale, expected dynamic brittle fracture features such as microcracking and crack branching are successfully captured. Similarly, [53] demonstrates the importance of using an inhomogeneous strength field for some dynamic fracture problems.

To accommodate material inhomogeneity at the RVE-level, we adopt a *numerical homogenization* approach, in that homogenized material properties are subsequently used as input parameters to a macroscopic problem. This process is depicted in fig. 1. The $800\,\mu\text{m}\times800\,\mu\text{m}$ RVE is covered by non-overlapping SVEs of a certain size. Through the homogenization of an SVE, for any given field, a value is assigned at the centroid of SVEs. These values are used to linearly interpolate the given field at any other point in the original domain. The second subfigure in fig. 1 shows a fracture strength field constructed based on a $1/32 \times 1/32$ division of RVE. Thus, this process can be viewed as an averaging and upscaling of microscale properties to within a level of inhomogeneity determined by the size of SVEs used to subdivide the RVE; the finer the SVEs, the more variation of material properties are maintained in constructed homogenized fields.

In principle, elastic properties and angle-dependent strengths $\tilde{s}_n(\theta)$ and $\tilde{s}_s(\theta)$, homogenized in SVEs, can be used to construct such homogenized fields for the macroscopic fracture analysis. However, in the present work first we only consider the inhomogeneity of fracture properties. This is justified by less variations of homogenized elastic properties, which will become evident in §4. In addition, fracture strength has been the field that is considered inhomogeneous in majority of similar studies, see for example [54, 55, 56, 57, 53].

Moreover, instead of maintaining the angular dependency of fracture strengths, we use $\tilde{S}_n$ and $\tilde{S}_s$, defined by,

$$\tilde{S}_n := \min_{\theta\in[0,\ \pi]}\tilde{s}_n(\theta), \tag{5a}$$

$$\tilde{S}_s := \min_{\theta\in[0,\ \pi]}\tilde{s}_s(\theta). \tag{5b}$$

as conservative minimum values of $\tilde{s}_n(\theta)$ and $\tilde{s}_s(\theta)$ over all angles of loading; note that $\tilde{s}_n(\theta+\pi) = \tilde{s}_n(\theta)$ and $\tilde{s}_s(\theta+\pi) = \tilde{s}_s(\theta)$. Finally, to further simplify the macroscopic analysis, only $\tilde{S}_n$ is treated as inhomogeneous and instead of a space- and angle-dependent mode mixity β (4), its mean value over all space and angle positions is considered. As will be observed in §4.3.1, this simplification is acceptable due to the weak anisotropy of fracture strengths.

Finally, we clarify that the damage model from §2.2 is only partially calibrated, because from its two *intrinsic scales* of *strength* $\tilde{S}_n$ and *time* $\tilde{\tau}$ only $\tilde{S}_n$ is treated as an inhomogeneous field. Given that *fracture energy* $\tilde{\phi}$ scales linearly with the product of fracture strength and time scales, *cf.* [58], this implies that by taking a constant value for $\tilde{\tau}$, $\tilde{\phi}$ proportionally varies with $\tilde{S}_n$. The same type of approximation is observed in TSR-based models in [55, 56, 57, 53] where again $\tilde{S}_n$ is treated as inhomogeneous, while the *intrinsic separation* of TSR is considered constant. Similar to the proposed damage model, $\tilde{\phi}$ linearly scales with $\tilde{S}_n$ for these TSR-based models. Note that ideally both intrinsic scales of an interfacial fracture model should be homogenized. However, it has been shown in [53] that even by considering $\tilde{S}_n$ alone to be inhomogeneous, realistic fragmentation patterns are captured and macroscopic measures such as ultimate load and fracture energy are rather insensitive to the macroscopic mesh gradation and the scale at which inhomogeneity is considered.

2.4. Mesh-adaptive aSDG method for macroscopic fracture analysis

At the macroscale a crack is nucleated at a position such as N in fig. 3 if the condition $\breve{s}(\theta) \geq \tilde{s}_n(\theta)$ holds for any angle $\theta \in [0, 2\pi)$. Similarly, an existing crack propagates from its tip, such as position Q in fig. 3, at an angle θ_0 for which $\breve{s}(\theta_0)/\tilde{s}_n(\theta_0)$ takes a maximum value greater than unity over all angles $\theta \in [0, 2\pi)$. These are collectively called the *principal of maximum effective circumferential stress* for crack nucleation and propagation. Once a crack propagates, the evolution model (3) is used to determine the rate at which D increases to unity to model the process of interface debonding. For all processes of crack nucleation, propagation, and damage evolution on existing crack surfaces, rather than $\tilde{s}_n(\theta)$, $\breve{s}(\theta)$ is compared against the angle-independent and inhomogeneous strength $\tilde{S}_n$.

A major challenge in computational dynamic fracture is tracking complex fracture patterns such as those shown in the last subfigure in fig. 1. *Extended Finite Element Methods* (XFEMs) [59, 60], *Generalized Finite Element Methods* (GFEMs) [61, 62], and *Discontinuity-Enriched Finite Element*

Methods (DE-FEMs) [63] are a few of the approaches that enrich the element solution space to model the crack propagation, nucleation, and bifurcation within elements. Herein, we take a different approach, where by mesh adaptive operations in spacetime, element boundaries are aligned with proposed crack propagation directions [64].

We employ the *asynchronous Spacetime Discontinuous Galerkin* (aSDG) method [65] for macroscopic dynamic fracture simulations. Various error indicators and spacetime adaptive operations ensure the accuracy of results. Dual error indicators in the bulk and on fracture interfaces control the energy dissipation and satisfaction of fracture constitutive relations, respectively [66]. The h-adaptive scheme [67] adjusts element sizes in the spacetime to efficiently satisfy the two aforementioned error conditions. Finally, cracks are nucleated at vertices of the space domain when the effective stress (2) reaches the (inhomogeneous) value of $\tilde{S}_n$ sampled at a given vertex. The principal of maximum effective circumferential stress is employed to determine the direction of crack propagation. The latter set of adaptive operations are particularly critical in capturing realistic fracture patterns. A more detailed review of this adaptive method for fracture simulations and its comparison with aforementioned enriched methods can be found in [12].

3. Microscopic analyses

3.1. Automated mesh generation

The domain shown in fig. 2, with edge size $L = 800$ μm, is used for the construction of SVEs. Square SVEs are constructed with four different edge sizes of $l_{\text{SVE}} = 12.5$ μm, 25 μm, 50 μm, and 100 μm. The non-dimensional size of an SVE is defined as,

$$l := \frac{l_{\text{SVE}}}{L}. \tag{6}$$

Thus, the non-dimensional sizes of sampled SVEs are $\frac{1}{64}$, $\frac{1}{32}$, $\frac{1}{16}$, and $\frac{1}{8}$. For these sizes, the RVE is divided into 4096, 1028, 256, and 64 SVEs, respectively.

The homogenization-based fracture analysis presented in §4 relies on the FE approximation of the stress field in all the 5440 SVEs sampled above. Clearly, performing such a large number of simulations would not be feasible without an utter automation of the modeling process, *i.e.,* converting the geometrical model corresponding to each SVE into an appropriate conforming mesh. Further, it is equally important to create a high-quality conforming

mesh for each SVE (small element aspect ratios and negligible discretization error) to accuracy approximate sites of stress concentrations along material interfaces. It is also highly desirable that the mesh is adaptively refined in such regions to maintain an acceptable computational cost without compromising the accuracy.

In order to automatically generate a high fidelity FE model for each SVE, we implement a new non-iterative mesh generation algorithm named Conforming to Interface Structured Adaptive Mesh Refinement (CISAMR) [37, 39]. In 2D, CISAMR transforms a structured mesh composed of quadrilateral elements into a conforming mesh, in which element aspect ratios are guaranteed to be less than 3. This is achieved by overlaying the domain geometry (*e.g.,* ZrB_2-SiC SVE) with a structured mesh, where CISAMR can automatically detect background elements intersecting with material interfaces, as well as relative position of mesh nodes with respect to each phase (*e.g.,* inside or outside of a particle). The transformation of the initial grid into a conforming mesh occurs in three steps: (i) h-adaptive refinement of background elements in the vicinity of material interfaces; (ii) r-adaptivity of nodes of elements cut by each interface, during which some of the nodes are moved to the interface while others maintain their original position; (iii) subdividing nonconforming elements, as well as elements with hanging nodes (created during the h-adaptivity phase) to build the final conforming mesh. It must be noted that in order to facilitate the homogenization-based fracture analysis presented in this article, the last phase is extended to all background quadrilateral elements to obtain a mesh composed of triangular elements only.

Figure 4 illustrates a small sub-region of the conforming mesh created for one of the SVEs studies in this work, which clearly shows proper aspect ratios of resulting elements in the vicinity of material interfaces. For this SVE and all SVEs studied in the following sections, initial structured meshes with an element size of $h = 1$ μm and two levels of h-adaptive refinement along particle-matrix interfaces are employed to generate corresponding conforming meshes. Note that additional levels of refinement might be necessary in regions where two material interfaces are in close proximity to properly capture stress concentrations in such areas. It is evident that CISAMR can highly facilitate the current homogenization-based study by enabling the automated construction of FE models for thousands of SVEs, which only requires overlaying a structured mesh corresponding to each SVE size with different regions of RVE shown in fig. 2a.

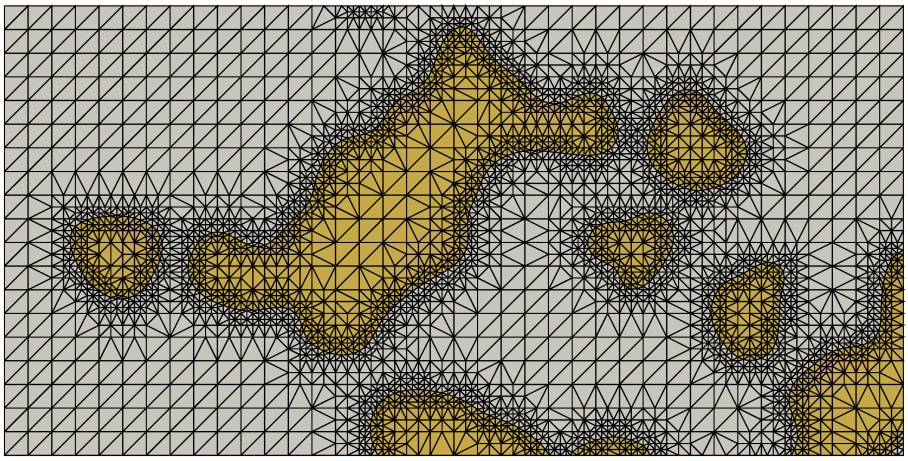

Figure 4: Small subset of the conforming mesh generated using CISAMR for one of the SVEs corresponding to the RVE microstructure depicted in fig. 2a.

3.2. Boundary conditions

Analyzing the micromechanical behavior of an SVE subject to a macroscopic load requires applying appropriate boundary conditions (BCs) to properly simulate the effect of this load. According to the homogenization theorem, such BCs must satisfy the strain averaging theorem [68, 69], which can be expressed as,

$$\boldsymbol{\varepsilon}_{\mathrm{M}}(\mathbf{x}_{\mathrm{M}}) = \frac{1}{|\Theta|}\int_{\Theta} \boldsymbol{\varepsilon}_{\mathrm{m}}(\mathbf{x}_{\mathrm{m}})\,\mathrm{d}\Theta, \tag{7}$$

meaning the corresponding macroscopic strain ε_{M} at point $\mathbf{x}_{\mathrm{M}}$ must be equal to the average of microscopic strains $\boldsymbol{\varepsilon}_{\mathrm{M}}$ in the corresponding SVE. Most straightforward choices that satisfy this theorem are the traction $\mathbf{t}_{\mathrm{m}}$ and displacement $\mathbf{u}_{\mathrm{m}}$ BCs applied along external edges Λ of SVE to represent $\boldsymbol{\varepsilon}_{\mathrm{M}}$ as,

$$\mathbf{t}_{\mathrm{m}}|_{\Lambda} = \mathbb{C}\boldsymbol{\varepsilon}_{\mathrm{M}}\mathbf{n}_{\mathrm{m}}, \quad \mathbf{u}_{\mathrm{m}}|_{\Lambda} = \boldsymbol{\varepsilon}_{\mathrm{M}}\mathbf{x}_{\mathrm{m}}, \tag{8}$$

where $\mathbb{C}$ is the fourth order elasticity tensor, $\mathbf{n}_{\mathrm{m}}$ is the outward unit normal vector to the SVE boundary, and $\mathbf{x}_{\mathrm{m}}$ is the microscopic coordinate. For SVEs subject to displacement BCs simulating a macroscopic normal stress, a traction-free BC is applied along lateral edges of the domain to minimize stress concentrations in these regions. In the remainder of this manuscript, we refer to this boundary condition as mixed BC.

While implementing either traction or mixed BCs in an FE model to simulate the micromechanical behavior of SVE is straightforward, unrealistic stress concentrations caused by such BCs in the vicinity of domain boundaries could undermine the accuracy [70]. Alternatively, it has been shown that using the periodic BC (PBC), together with applying ε_{M} to all elements of SVE (rather than applying its effect along domain boundaries), can considerably alleviate this problem [71]. However, a major limitation of PBC is that it can only be utilized in a periodic FE mesh, which in turn requires an SVE with a periodic microstructure. Thereby, because SVEs created as subdomains of the virtual RVE depicted in fig. 2a lack this characteristic, we cannot implement PBC in the present study.

As an alternative to PBC for problems with non-periodic microstructures, one can implement the Minimal Kinematics BC (MKBC) [72], in which ε_{M} is imposed on SVE edges in a weak sense, i.e.,

$$\boldsymbol{\varepsilon}_{\mathrm{M}_{ij}}(\mathbf{x}_{\mathrm{M}}) = \frac{1}{2|\Theta|}\int_{\Lambda}\left(u_{\mathrm{m}_i}n_{\mathrm{m}_j} - u_{\mathrm{m}_j}n_{\mathrm{m}_i}\right)\,\mathrm{d}\Lambda, \tag{9}$$

where $|\Theta|$ is the area of SVE and i, j are indicial notations. The following degrees of freedom are also constrained at arbitrary-selected nodes A and B on domain boundaries to prevent rigid body motion: $\mathbf{u}_{\mathrm{m}}^{\mathrm{A}} = \mathbf{0}$ and $u_{\mathrm{m}_2}^{\mathrm{B}} = 0$. More details regarding the implementation of MKBC, together with a comparison of its performance with PBC, is provided in [71].

A thorough study on the impact of different SVE sizes and BCs (mixed, traction, and MKB) on corresponding PDFs, as well as the homogenization-based fracture response of RVE is presented in §4. As a prelude to this study, fig. 5 shows a comparison between FE approximations of the normal stress field in the x-direction (σ_{xx}) in an SVE with $l_{\mathrm{SVE}} = 50$ μm subject to mixed BC, traction BC, and MKBC representing a macroscopic tensile stress in the same direction. This figure also illustrates normal stress fields in four smaller SVEs with $l_{\mathrm{SVE}} = 25$ μm subject to different BCs, each of which is a quadrant of the SVE with $l_{\mathrm{SVE}} = 50$ μm. In each case, a unit value of corresponding BC (i.e., unit displacement, traction, or macroscopic strain) is applied to SVE. Resulting stress field are then normalized to have the same range. Note that ranges of σ_{xx} in color bars associated with mixed BC compare to traction BC and MKBC are quite similar. However, focusing on the left edge of SVE with $l_{\mathrm{SVE}} = 50$ μm, it is evident that using mixed BC leads to more pronounced stress concentrations in this region. For all BCs, differences between stress fields away from the domain edges are negligible,

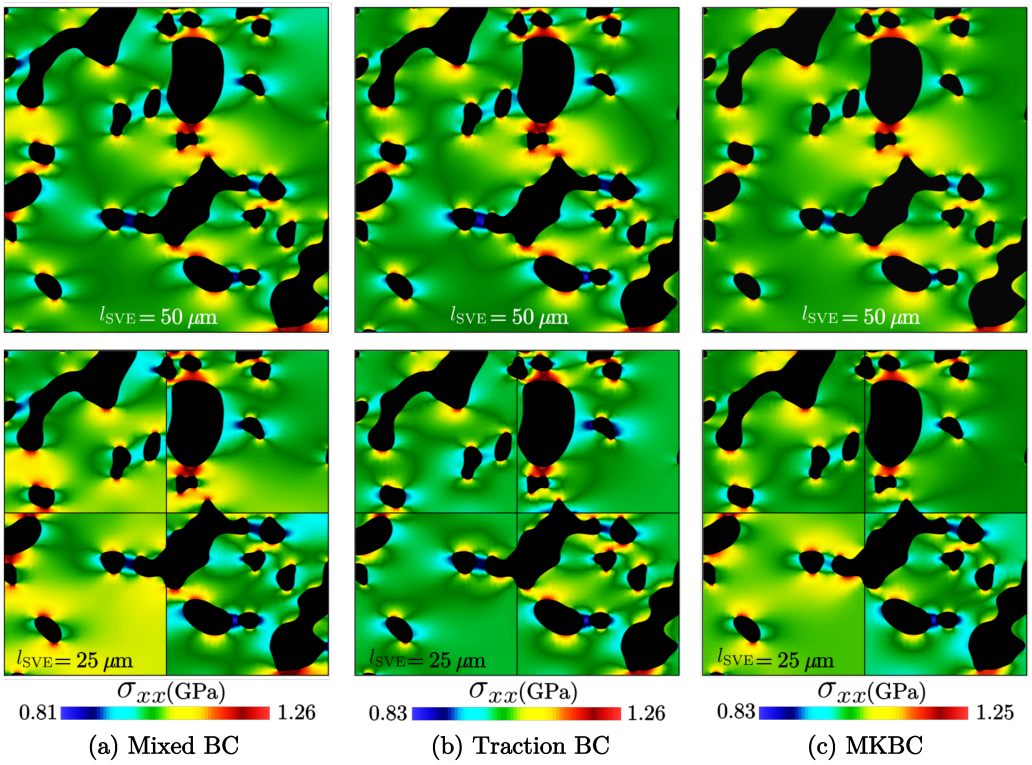

(a) Mixed BC (b) Traction BC (c) MKBC

Figure 5: Comparison between FE approximations of σ_{xx} in an SVE with $l_{\text{SVE}} = 50\ \mu$m and four smaller SVEs corresponding to its quadrants with $l_{\text{SVE}} = 25\ \mu$m under mixed and traction BCs replicating a macroscopic strain applied in the x-direction.

which reemphasizes the fact that increasing the SVE size mitigates the role of the type of BC on predicted average stresses.

Studying stress fields in smaller SVEs ($l_{\text{SVE}} = 25\ \mu$m) in fig. 5 sheds more light on the impact of different BC types on the simulated micromechanical behavior. Because each quadrant SVE is analyzed independently, the normal stress along midlines of the resulting contour plot is discontinuous. More pronounced stress concentrations along edges of SVEs subject to mixed BC compared to those analyzed using MKBC and traction BC is also evident in the figure. More insight into the impact of BC type on the stress field can be obtained by comparing contour plots of the large SVEs ($l_{\text{SVE}} = 50\ \mu$m) with those created by putting together the smaller SVEs representing its quadrants. In particular, stress fields in the lower two quadrant SVEs ($l_{\text{SVE}} =$

25 μm) simulated under mixed BC show a notable discrepancy with the FE approximation of the normal stress in the lower half of large SVE.

It is worth mentioning that, as will be shown in §4, homogenized values for elastic moduli and fracture strengths evaluated for SVEs simulated under traction BC and MKBC assumption will be identical. At first glance, this might seem contradictory, as in MKBC a unit macroscopic strain is weakly imposed in one direction (*e.g.,* in x), while a zero macroscopic strain is maintained in other directions (*e.g.,* in y and xy). On the other hand, applying a normal traction BC in the same direction causes normal strain in the perpendicular direction due to the Poisson's effect, which would clearly not be identical to that obtained from MKBC. Note that this difference is confirmed by the stress field depicted in fig. 5, where σ_{xx} fields associated with traction BC and MKBC are not identical. However, since both simulations are conducted under linear elastic assumption, the stress field approximated under normal traction BC is in fact a superposition of that evaluated using MKBC in x and y directions; hence resulting homogenized material properties would be the same. This indicates the superiority of traction BC over MKBC for linear homogenization analyses, as imposing the constraint (9) for a simulation under MKBC leads to a high condition of the stiffness matrix, which in turn leads to a higher computational cost and implementation complexities. Note that this would not be the case if one aims to perform a nonlinear simulation involving plasticity or damage, where linear superposition is no longer valid.

3.3. Effective fracture strength

3.3.1. Angle-dependency of fracture strengths

In this section, we present the derivation of the elasticity stiffness tensor and angle-dependent tensile and shear fracture strengths of SVEs. For any of the square SVEs and any of the three BCs discussed in §3.2, the linear and static FE approximations are carried out subject to three load cases to derive corresponding homogenized elasticity and fracture values. The average macroscopic stress tensor, in Voight notation, for the load case number α can be written as,

$$\bar{\boldsymbol{\sigma}}^{\alpha} = [\bar{\sigma}^{\alpha}_{xx}, \bar{\sigma}^{\alpha}_{yy}, \bar{\sigma}^{\alpha}_{xy}]^{\intercal}, \quad \alpha \in \{1, 2, 3\}, \tag{10}$$

where $^{\intercal}$ is the transpose operator. For example, for traction BC, these three load cases are proportional to $[1, 0, 0]^{\intercal}$, $[0, 1, 0]^{\intercal}$, and $[0, 0, 1]^{\intercal}$. Having the average strains and stresses from these three load cases enables computation

of the potentially anisotropic homogenized stiffness and compliance matrices, as well as the in-plane bulk modulus.

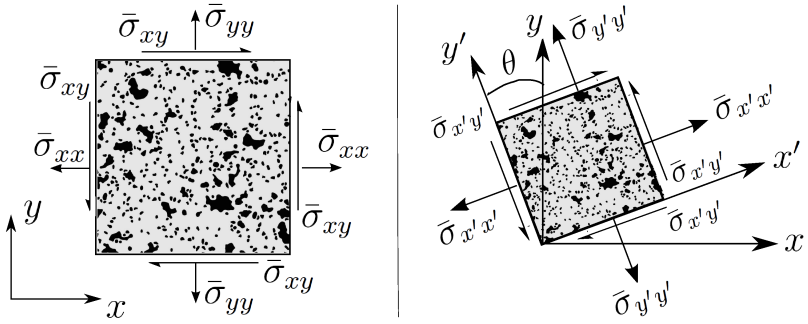

Figure 6: Schematic of an SVE in the global (x, y) and local (x', y') coordinate systems used for defining fracture strengths at an angle θ.

Figure 6 shows the schematic of an SVE in the global coordinate system (x, y). The local coordinate (x', y') is obtained by rotating (x, y) by angle θ in the counter clockwise direction. Stress components in the (x, y) coordinate system are obtained by those in the rotated (x', y') coordinate system by using the Mohr circle relations [42],

$$\bar{\sigma}_{xx} = \frac{\bar{\sigma}_{x'x'} + \bar{\sigma}_{y'y'}}{2} + \frac{\bar{\sigma}_{x'x'} - \bar{\sigma}_{y'y'}}{2}\cos(2\theta) - \bar{\sigma}_{x'y'}\sin(2\theta) \tag{11a}$$

$$\bar{\sigma}_{yy} = \frac{\bar{\sigma}_{x'x'} + \bar{\sigma}_{y'y'}}{2} - \frac{\bar{\sigma}_{x'x'} - \bar{\sigma}_{y'y'}}{2}\cos(2\theta) + \bar{\sigma}_{x'y'}\sin(2\theta) \tag{11b}$$

$$\bar{\sigma}_{xy} = \frac{\bar{\sigma}_{x'x'} - \bar{\sigma}_{y'y'}}{2}\sin(2\theta) + \bar{\sigma}_{x'y'}\cos(2\theta) \tag{11c}$$

To obtain $\tilde{s}_n(\theta)$, the normal strength of an SVE at angle θ, an average stress loading is sought where $\bar{\sigma}_{y'y'} = \tilde{s}_n(\theta)$, $\bar{\sigma}_{x'x'} = 0$, and $\bar{\sigma}_{x'y'} = 0$. The value of $\tilde{s}_n(\theta)$ is chosen such that the failure can be initiated in the matrix, inclusion, or their interface as described below. The reason that $\bar{\sigma}_{y'y'}$ rather than $\bar{\sigma}_{x'x'}$ is set to be equal to the strength at angle θ is that if a crack is nucleated at this point, it has an orientation of θ with respect to the x axis. For the angle-dependent shear strength $\tilde{s}_s(\theta)$, average stresses in the (x', y') coordinate are $\bar{\sigma}_{x'x'} = 0$, $\bar{\sigma}_{y'y'} = 0$, and $\bar{\sigma}_{x'y'} = \tilde{s}_s(\theta)$. From (11) the stress conditions corresponding to normal and shear loadings at angle θ are factors

of

$$\bar{\boldsymbol{\sigma}}_n(\theta) = [\sin^2(\theta), \cos^2(\theta), -\sin(\theta)\cos(\theta)]^\intercal, \tag{12a}$$

$$\bar{\boldsymbol{\sigma}}_s(\theta) = [-\sin(2\theta), \sin(2\theta), \cos(2\theta)]^\intercal. \tag{12b}$$

For any of the BC modes considered in this manuscript, the three averaged solutions $\bar{\boldsymbol{\sigma}}^\alpha$ corresponding to the load cases used for the homogenization provide a basis to span the stress space. Thus, by a linear combination of them either of the stress states $\bar{\boldsymbol{\sigma}}_n(\theta)$ or $\bar{\boldsymbol{\sigma}}_s(\theta)$ can be formed to represent a normal or shear average stress loading at angle θ, respectively. For the superposition of $\bar{\boldsymbol{\sigma}}^\alpha$ that forms $\bar{\boldsymbol{\sigma}}_n(\theta)$, the microscopic stress values are determined at each point in the matrix, inclusions, and their interfaces. Failure models for each of the three phases of matrix, inclusion, and interface will be discussed in the next section. Knowing these failure models, we can find the smallest load factor to (12a) loading for which failure is initiated at least in one of the phases. This load factor corresponds to *fracture initiation strength* for a normal tensile loading corresponding to θ, which is associated with the normal strength $\tilde{s}_n(\theta)$. The same process is used to derive $\tilde{s}_s(\theta)$ from $\bar{\boldsymbol{\sigma}}_s(\theta)$ in (12b). In §4.3.1, it will be shown that strengths $\tilde{s}_n(\theta)$ and $\tilde{s}_s(\theta)$ become more isotropic as the SVE size increases. Except that section, we will only analyze the statistics of $\tilde{S}_n$ and $\tilde{S}_s$; *cf.* (5).

The aforementioned linear analysis at the SVE level only provides $\tilde{S}_n$ and $\tilde{S}_s$. For a variety of interfacial fracture models, *e.g.,* the damage model from §2.2 and *extrinsic* TSRs, they provide the stress level beyond which debonding initiates. To fully formulate and calibrate a macroscopic interfacial model, however, the entire stress response versus macroscopic fields (*e.g.,* displacement jump for TSRs) is required. This entails a nonlinear analysis of VE for stress levels beyond $\tilde{S}_n$ and $\tilde{S}_s$, for which cracks or other forms of weakening processes initiate from the most critical points. It is only through the analysis of their propagation and coalescence that the energy characteristic and the nonlinear response of the interfacial model to full debonding can be characterized.

Limiting our SVE failure analysis to the derivation of $\tilde{S}_n$ (and $\tilde{S}_s$) is acceptable as the only input(s) for the macroscopic fracture model in §2.2. First, $\tilde{S}_n$ and $\tilde{S}_s$ serve the purpose of generating an inhomogeneous field for fracture strength, which as demonstrated in [54, 55, 56, 57, 53] can capture key characteristics of brittle fracture. The advantage of the current approach is that SVEs, rather than phenomenological models such as Weibull distribution, are used to assign $\tilde{S}_n$ at the RVE-level. Second, since quasi-brittle

materials lack the large energy dissipation capacity of ductile materials, their nonlinear response past $\tilde{S}_n$ is less pronounced. This is reflected in rather close values for $\tilde{S}_n$ and *ultimate strength* based on the quasi-static analysis of VEs in [73]. This proximity is observed even for strain rates up to around 10^4/s in [53], implying that only calibrating $\tilde{S}_n$ for an interfacial fracture model is deemed satisfactory for up to relatively moderate loading rates. Third, the model (3) is already rate-sensitive and predicts higher ultimate strength and fracture energy as the loading rate increases. This is qualitatively consistent with the observations made from fully nonlinear analysis of VEs in [53] for strain rates beyond 10^4/s.

3.3.2. Failure criteria

As described in §3.3.1, $\tilde{s}_n(\theta)$ and $\tilde{s}_s(\theta)$ correspond to averaged normal and shear stresses at angle θ, *cf.* fig. 6, such that failure is about to initiate at a point in the matrix, inclusions, or interfaces between the two. In this section, we describe the failure criteria used in each of these three phases. This determines that for a given point how much larger the unit normal and shear loadings in (12) can be to initiate failure. Thus, by determining the most critical point, $\tilde{s}_n(\theta)$ and $\tilde{s}_s(\theta)$ are determined.

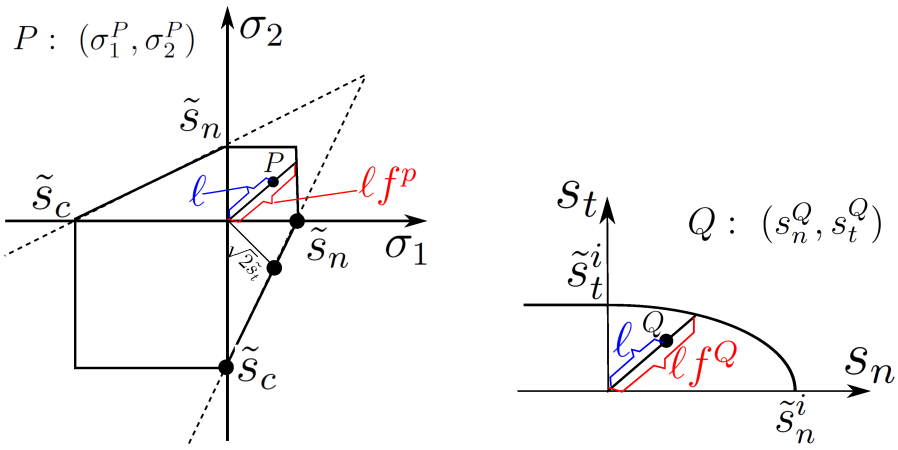

(a) Mohr Coulomb bulk failure criterion (b) Interfacial failure criterion [49]

Figure 7: Bulk and interfacial failure criteria used to compute the angle-dependent fracture strengths of an SVE. In a) the dashed line corresponds to unmodified Mohr-Coulomb criterion, and the solid region corresponds to the modified criterion used herein.

The solid line in fig. 7a shows the modified isotropic Mohr-Coulomb failure criterion in the 2D principal stress space. The Mohr-Coulomb model is characterized by the uniaxial tensile $\tilde{s}_n$ and uniaxial compressive $\tilde{s}_c$ strengths. Corresponding strengths for the two phases are decorated by a superscript $\alpha \in \{M, I\}$ corresponds to "Matrix" and "Inclusion" phases. Thus, $\tilde{s}_n^M$ and $\tilde{s}_c^M$ are uniaxial tensile and compressive strengths of the (ZrB_2) matrix phase, and $\tilde{s}_n^I$ and $\tilde{s}_c^I$ are corresponding values for the (SiC) inclusion phase, respectively.

The dashed lines in fig. 7a correspond to an unmodified Mohr-Coulomb model which is often characterized by the friction coefficient and cohesion parameters. However, such model overestimates the hydrostatic tensile strength and predicts a wrong fracture angle [11]. In addition, it has no limit on hydrostatic compressive stress. There are various modified Mohr-Coulomb models, *e.g.,* the Hoek-Brown model [74], but the model used in fig. 7a is simple yet addresses the aforementioned shortcomings. In addition, it predicts the same value for uniaxial and hydrostatic tensile strengths. Finally, from fig. 7a the shear strength is derived as,

$$\tilde{s}_c = \frac{\tilde{s}_n \tilde{s}_c}{\tilde{s}_n + \tilde{s}_c}. \tag{13}$$

For the analysis of fracture initiation along interfaces between the matrix and inclusion phases, we employ the scalar effective stress proposed by [49],

$$\breve{s} = \sqrt{\langle s_n \rangle^2 + (\beta s_s)^2}, \tag{14}$$

where β is the mode mixity parameter, and s_n and s_s are normal and shear components of the traction vector acting on an interface.[1] The failure criterion for an interface, $\tilde{s} = \tilde{s}_i$ is shown in fig. 7b, where $\tilde{s}_i$ is the strength of the interface. Based on the form of (14) the normal and shear strengths of the interface are $\tilde{s}_n^i = \tilde{s}_i$ and $\tilde{s}_s^i = \tilde{s}_i/\beta$.

The use of these failure criteria in the determination of $\tilde{s}_n(\theta)$ is as follows. From (12a), the macroscopic (average) SVE stress array $\bar{\boldsymbol{\sigma}}_n(\theta)$ corresponds to the tensile stress $\bar{\sigma}_{y'y'}$ of magnitude one. As mentioned in §3.3.1, the superposition of the three load cases of an SVE is done such that the superposed

[1] Equations (14) and (2) are effective stresses in the form proposed by [49]. However, (14) is utilized along interfaces between the matrix and inclusions in each SVE, while (2) is used at the RVE-scale and is compared to homogenized fracture strength $\tilde{S}_n$.

average macroscopic stress from $\bar{\boldsymbol{\sigma}}^{\alpha}$ is equal to $\bar{\boldsymbol{\sigma}}_n(\theta)$. Thus, the microscopic stress state for all points of SVE corresponding to the macroscopic loading $\bar{\boldsymbol{\sigma}}_n(\theta)$ is known. Figure 7a shows the principal stress state (σ_1^P and σ_2^P) in a sample point P in one of the two bulk phases. As shown, if the macroscopic loading $\bar{\boldsymbol{\sigma}}_n(\theta)$ is multiplied by f^P, fracture initiates at the point P. Similarly, the traction components for a point Q at the interface between the two phases is shown fig. 7b. For this point, the load factor f^Q is required to initiate fracture. Thus, by taking minimum values of f^P and f^Q over all points in bulk phases and their interfaces we find the smallest load required to initiate fracture in SVE. Given that $\bar{\sigma}_{y'y'} = 1$ for $\bar{\boldsymbol{\sigma}}_n(\theta)$, this load factor in fact corresponds to $\tilde{s}_n$, the tensile fracture initiation strength at angle θ. The same process is used for the superposed solution corresponding to $\bar{\boldsymbol{\sigma}}_s(\theta)$ in (12b) to obtain $\tilde{s}_s$. It is noted that a similar approach was implemented in [42], however therein a simplified model with circular inclusions was used for the composite and fracture initiation was restricted to the interface only.

4. Results and discussions

For the composite ZrB_2-SiC, material properties of the ZrB_2 matrix phase are: Young's modulus $E^M = 524$ GPa, Poisson's ratio $\nu^M = 0.15$, tensile strength $\tilde{s}_n^M = 381$ MPa, and compressive strength $\tilde{s}_c^M = 2.5$ GPa [75, 76, 77]. The inclusion phase, SiC, properties are: Young's modulus $E^I = 415$ GPa, Poisson's ratio $\nu^I = 0.15$, tensile strength $\tilde{s}_n^I = 359$ MPa, and compressive strength $\tilde{s}_c^I = 2.1$ GPa [78]. Employing (13), the shear strength of these two phases are obtained as $\tilde{s}_s^M = 330.6$ MPa and $\tilde{s}_s^I = 306.6$ MPa. A plane stress mode is used for the 2D analyses reported herein. The interface tensile strength is assumed to be 80% of the minimum of tensile strengths of matrix and inclusion phases, which is a reasonable assumption for composites of this type [79]. The interface fracture mode mixity is assumed to be one, that according to (14) implies that $\tilde{s}_n^i = \tilde{s}_s^i = 287$ MPa.

4.1. Volume ratio of inclusions

The volume fraction of SiC in the 800 μm $\times$ 800 μm domain is 20%; *cf.* fig. 2. However, the *microscopic volume ratio* of sampled SVEs, v_f, is not necessarily equal to the macroscopic value and has a certain probability distribution depending on the SVE size l. Figure 8 shows the (PDF) of SiC volume ratio for different SVE sizes. The largest variations are observed for

the smallest SVE size, $l = \frac{1}{64}$. As the SVE size increases, the PDFs become narrower and centered around 0.2, the volume ratio of the macroscopic domain.

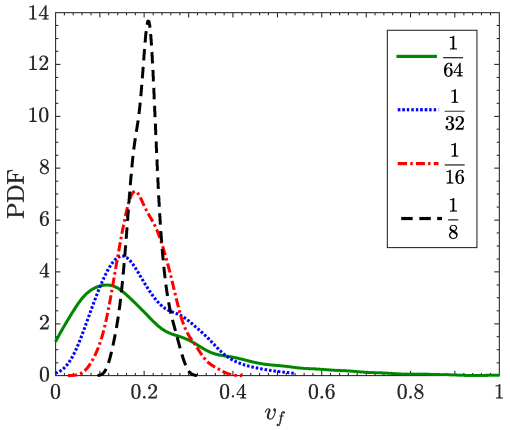

Figure 8: PDFs of v_f for $l = \frac{1}{64}, \frac{1}{32}, \frac{1}{16}$, and $\frac{1}{8}$.

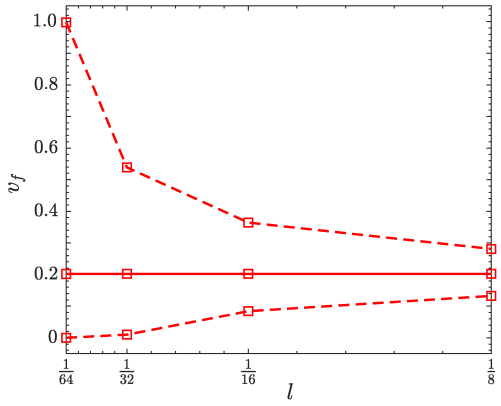

Figure 9: Minimum, maximum, and mean values of v_f versus l.

To better understand the distribution of v_f, the variation of its minimum, maximum, and mean values versus the SVE size is shown in fig. 9. For the smallest size $l = \frac{1}{64}$, the minimum volume ratio is identically zero. This corresponds to SVEs that do not intersect any of inclusions. Out of 4096 SVEs for this size, there are 60 SVEs with $v_f = 0$. On the other side of the spectrum, there are 4 SVEs with $v_f \geq 0.95$ and the largest volume ratio is $v_f = 0.998$, that is an SVE that is almost entirely composed of SiC particles. The high variation of v_f is a consequence of the natural clustering of inclusions, which is replicated using the multi-objective GA optimization phase of the reconstruction algorithm, as discussed in §2.1. The ranges of v_f are $[0.01,\ 0.54]$, $[0.08,\ 0.362]$, and $[0.13,\ 0.28]$, for $l = \frac{1}{32}$, $l = \frac{1}{16}$, and $l = \frac{1}{8}$, respectively. As demonstrated in the figure, mean values of v_f are very stable and for all SVE sizes and are equal to 0.2. This clearly is expected as SVEs of any size eventually cover the entire macroscopic domain with the volume ratio of 0.2.

4.2. Bulk modulus of SVEs

As described in §3.2, the elastic stiffness and compliance tensors can be characterized by the analysis of SVE for three different load cases. The *in-plane bulk modulus* is defined as the ratio of in-plane pressure to the relative

area change and is equal to,

$$\kappa = \frac{1}{\mathcal{C}_{11} + \mathcal{C}_{22} + 2\mathcal{C}_{12}}, \tag{15}$$

where $\mathcal{C}_{ij}$ are components of the potentially anisotropic compliance tensor in Voight notation.

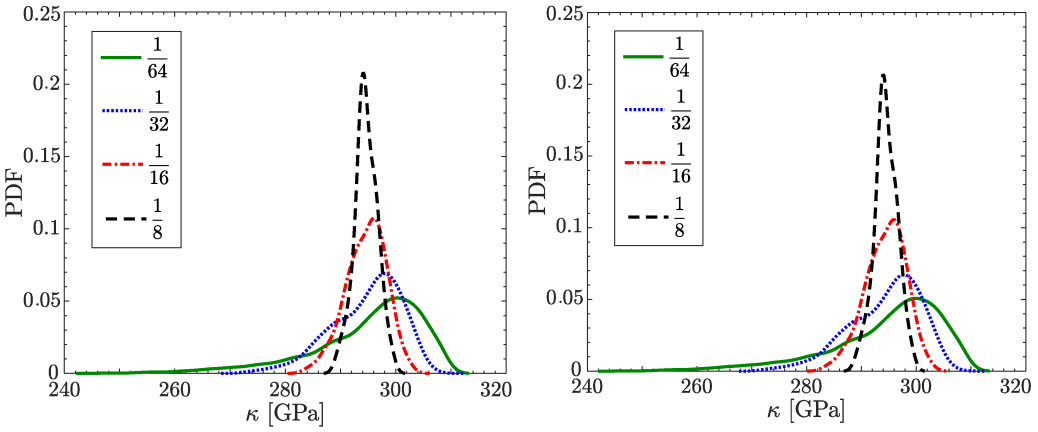

(a) Mixed BC (b) Traction BC

Figure 10: PDFs of bulk modulus for different SVE sizes analyzed by different BCs.

We investigate how the bulk moduli of SVEs are related to those of two phases. For an isotropic material, the in-plane bulk modulus is $2(1-2\nu)/E$ in the plane stress mode. Thus, bulk moduli of the matrix and inclusion are $\kappa^M = 308$ MPa and $\kappa^I = 248$ MPa, respectively. Figure 10 shows PDFs of κ for different SVE sizes and BC modes. First, it is observed that the bulk modulus is very insensitive to the choice of BC. Note that as mentioned previously, results for MKBC are identical to those from traction BC and thus not shown in the figures presented hereafter. Second, for $l = \frac{1}{64}$, the statistical variation in the homogenized bulk modulus falls between corresponding values of the two constituent phases. This is the reflection of the variation in the microscopic volume fraction shown in fig. 8, which spans almost the entire range of 0 to 1. Third, as the SVE size increases, PDFs shrink and their mean values approach the RVE limit bulk modulus. Also, through this process PDFs appear to become more symmetric and mode values decrease.

Figure 11 better demonstrates these trends. In fact, by using the statistics of κ and a power law relation between l_{SVE} and variations in the homogenized

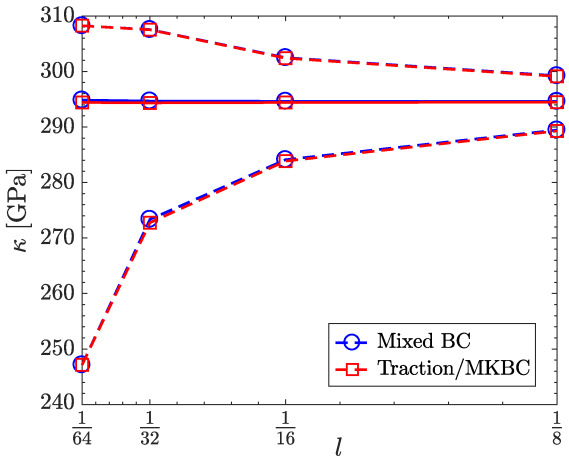

Figure 11: Minimum, maximum, and mean values of bulk modulus versus the SVE size l.

property [80, 81], only about 1% variation in homogenized κ is expected for a VE size of $l_{\text{SVE}} \approx 800$ μm. This condition is recommended in [14] in deciding the size of the RVE and matches the RVE size chosen for this analysis, that is $L = 800$ μm ($l = 1$).

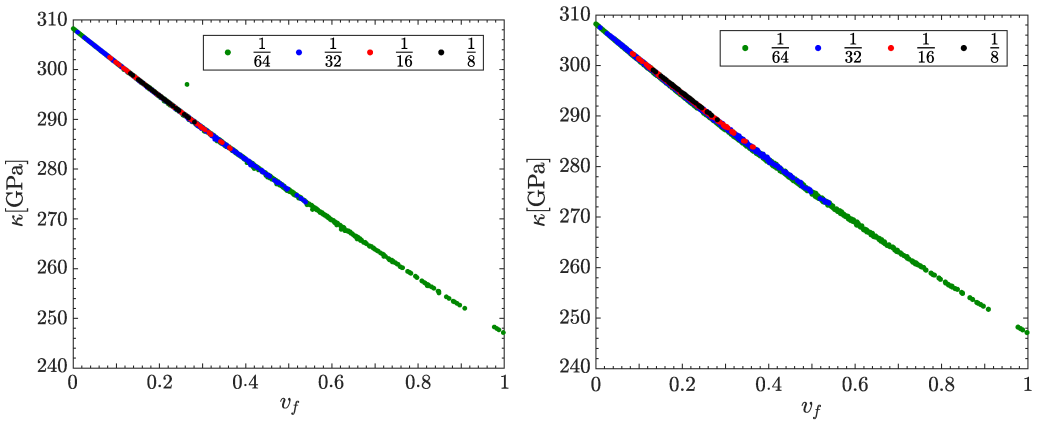

(a) Mixed BC (b) Traction BC

Figure 12: Variation of the bulk modulus as a function of the volume fraction for different SVE sizes.

To clarify the source of the variation of bulk modulus, κ is plotted versus v_f in fig. 12 for all SVE sizes. Elastic properties of an SVE are generally

affected by elastic properties of its constituents, their relative volume ratio, spatial arrangement of different phases, and the size of SVE. Herein, we observe that κ is a rather linear function of v_f for all SVE sizes. That is, there is almost no variations on κ for all realized SVEs with a given v_f. Variations for $l = \frac{1}{64}$ are slightly higher than those for larger SVE sizes, but even for smallest SVEs variations are minimal. Given the minimum and maximum values of v_f for this SVE size, *cf.* fig. 9, the corresponding bulk modulus varies from $\kappa^M = 308$ MPa to $\kappa^I = 248$ MPa as v_f ranges from unity to zero.

From this figure it is clear that the main source of lower variability of κ in fig. 10 is lower variations of v_f, *cf.* also fig. 9. In general, the particular distribution of inclusions even for the same v_f can have a noticeable impact on homogenized elastic properties. As the SVE size increases, two things happen; first v_f of SVEs gets closer to the macroscopic volume ratio, as shown in fig. 9, and second due to the large population of inclusions their geometric effect also balances out among different SVE realizations. Herein, we do not observe significant geometric effect even for smallest SVEs.

Another observation is the rather linear change of κ versus v_f. This effect is more pronounced for the mixed boundary condition, as for traction BC the relation is slightly convex. The Pearson correlation coefficients of 0.8573 and 0.8567 for mixed and traction BCs confirm this observation. The rather linear dependence of κ on v_f and its weak dependence on particular (geometric) representations of SVEs with the same v_f are consequences of the proximity of elastic moduli of two phases. It also explains the similarity of PDFs in fig. 8 and fig. 10 and the size effect plots in fig. 9 and fig. 11, for the fields v_f and κ. Finally, this almost linear response implies that the mean values of κ for all SVE sizes are very close and are approximately equal to 248 MPa, the linearly interpolated value of κ from the two phases based on the mean value of 0.2 for v_f.

4.3. Fracture strength of SVEs

4.3.1. Angle-dependency of fracture strengths

The process detailed in §3.3.1 is used to characterize $\tilde{s}_n(\theta)$ and $\tilde{s}_s(\theta)$ for all SVEs. The results for a sequence of four nested SVEs are shown in fig. 13 in that the SVE corresponding to fig. 13a is the lower left quadrant of the SVE corresponding to fig. 13b and so forth. Several observations can be made. First, in all cases the shear strength is lower than the normal strength. The smaller shear strength of both phases, *e.g.*, $\tilde{s}_n^M = 381$ vs. $\tilde{s}_s^M = 330.6$ MPa,

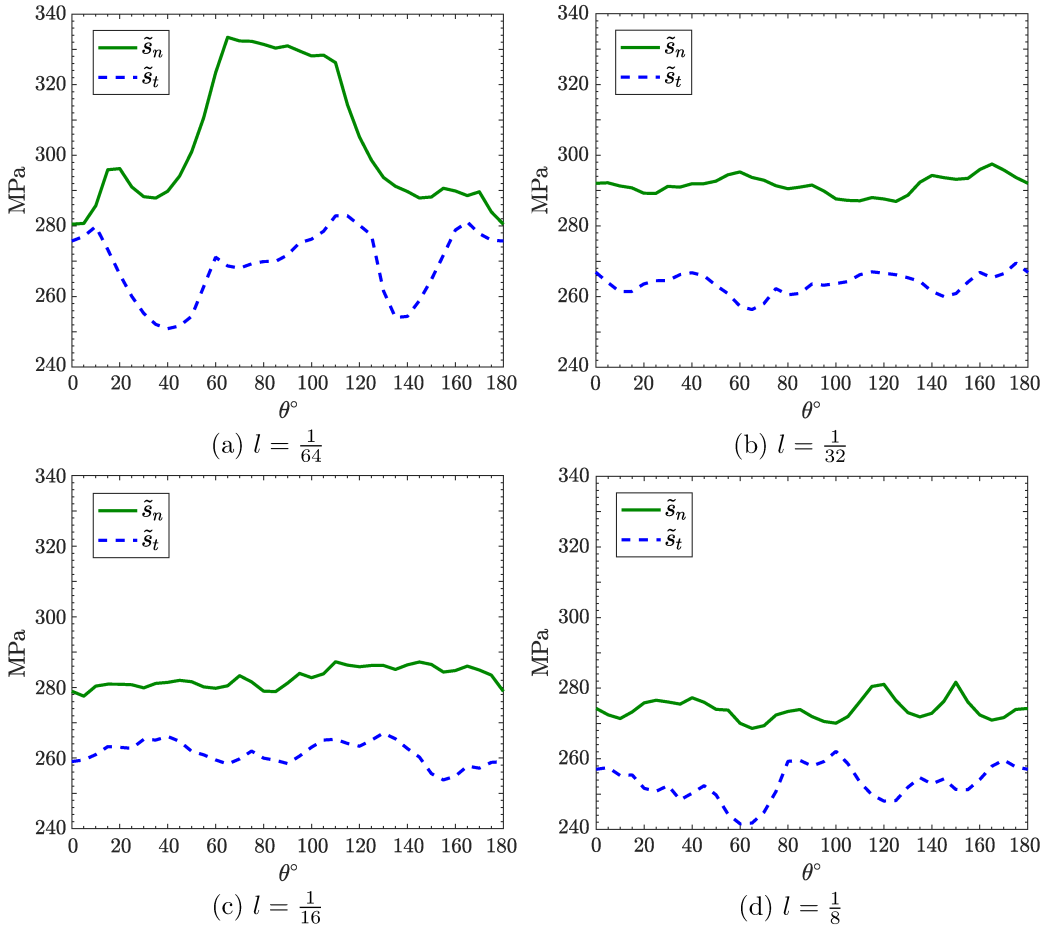

(a) $l = \frac{1}{64}$ (b) $l = \frac{1}{32}$

(c) $l = \frac{1}{16}$ (d) $l = \frac{1}{8}$

Figure 13: Variation of normal $\tilde{s}_n(\theta)$ and shear $\tilde{s}_s(\theta)$ strengths with load angle for sample SVEs with different sizes and traction BC.

the response of the interfacial fracture model, and the difference in stress distributions for normal and shear SVE loadings contribute to smaller $\tilde{s}_s$ than $\tilde{s}_n$.

The results for different SVE sizes also suggest the manner in which the fracture strengths vary as a function of l. First, there is an overall decrease to strengths. Second, the span of fracture strength, that is the difference between maximum and minimum strengths across all angles of loading, decreases for both $\tilde{s}_n$ and $\tilde{s}_s$ as the SVE size increases. For example, high anisotropy of strengths in fig. 13a is caused by positioning of a few inclusions close to one of the boundaries of the corresponding SVE; as l_{SVE} increases

more inclusions are included in the SVE, resulting in a more isotropic response. This effect holds for the elastic and fracture properties and is reported herein for fracture strengths. From here we focus on the conservative strengths $\tilde{S}_n$ and $\tilde{S}_s$ defined in (5).

4.3.2. Zone of fracture initiation

As discussed in §3.3.2, fracture can initiate in the bulk or in the matrix, both based on the Mohr-Coulomb fracture model. In addition, fracture can initiate along interfaces based on the definition of effective stress (14). As our results demonstrate, for the material considered, almost no failure is initiated in the inclusion phase for either normal or shear strength evaluations. Thus, only the percentages of failure in the matrix and interface phases are shown in fig. 14 and fig. 15 corresponding to $\tilde{S}_n$ and $\tilde{S}_s$, respectively. We first study the dominant zone of failure for normal strength in fig. 14. For the SVE size $l = \frac{1}{64}$, the failure is almost entirely initiated in the interface, except 2.39% and 2.29% of failures being initiated in the matrix for mixed and traction BCs, respectively. The very small percentage of failures in the bulk are associated with SVEs containing no inclusion (hence no interfaces), comprising $\approx 1.5\%$ of SVEs of this size, as well as SVEs with very low v_f. For $l = \frac{1}{32}$, the matrix failure percentage drops further to 0.1% and 0.03% for mixed and traction BCs, respectively. For all larger SVEs, this percentage is zero.

The failure zone percentages for the shear strength $\tilde{S}_s$ are presented in fig. 15. It is observed that failure initiates in the matrix phase for a significantly larger percentage of SVEs compared to that for $\tilde{S}_n$. Under macroscopic normal and shear loading the local stress state within the two bulk phases are also mostly in normal and shear modes, except at some locations in the vicinity of the inclusions. The interface tensile and shear strengths $\tilde{s}_n^i = \tilde{s}_s^i = 359$ MPa are much closer to shear strengths of the bulk phases ($\tilde{s}_s^M = 330.6$ MPa and $\tilde{s}_s^I = 306.6$ MPa) than their tensile strengths ($\tilde{s}_n^M = 381$ MPa and $\tilde{s}_n^I = 359$MPa). Thus, the fracture is more likely to initiate in the bulk phases under a shear loading compared to a tensile loading on an SVE. This explains higher percentages of the failure in the matrix case in fig. 15 compared to fig. 14. As for the results of mixed BC in fig. 15a, a higher rate of failure is observed in the matrix compared to fig. 15b.

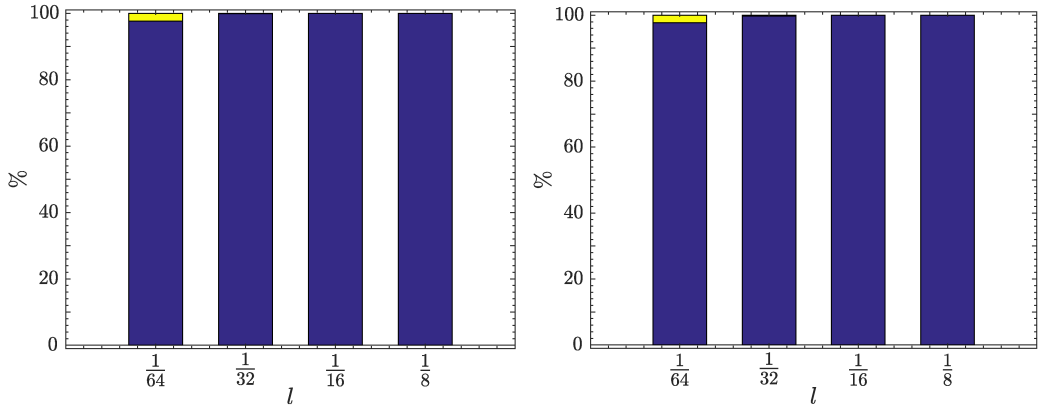

(a) Mixed BC (b) Traction BC

Figure 14: Distribution of failure zones for the tensile strength $\tilde{S}_n$ using mixed and traction BCs. Yellow and dark blue colors correspond to failure in the matrix and interface phases, respectively.

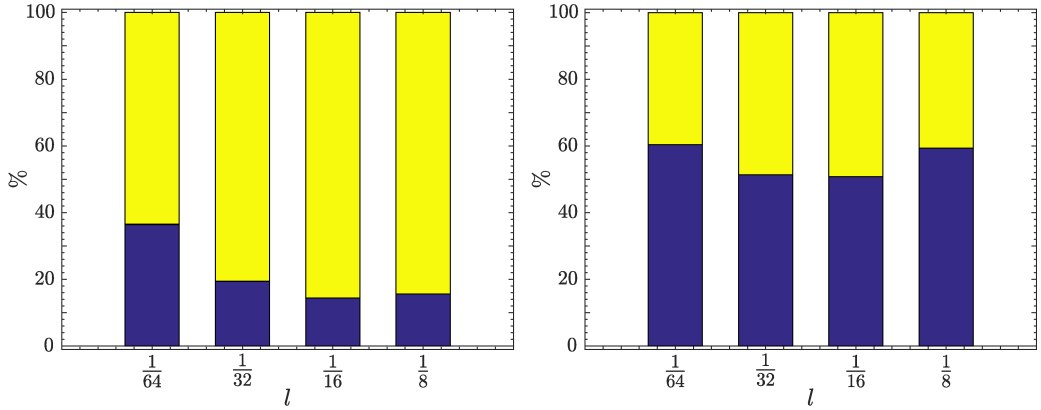

(a) Mixed BC (b) Traction BC

Figure 15: Distribution of failure zones for the shear strength $\tilde{S}_s$ using mixed and traction BCs. Yellow and dark blue colors correspond to failure in the matrix and interface phases, respectively.

4.3.3. Dependence of fracture strength on volume fraction

Due to the importance of v_f on homogenized properties, as shown for κ in §4.2, we first study its impact on fracture strengths. Normal and shear fracture strengths for the entire data set for the mixed BC are plotted versus v_f in fig. 16. The singleton points corresponding to $v_f = 0$ in both plots

correspond to about 1.5% of SVEs with $l = \frac{1}{64}$ that are entirely comprised of the matrix, thus exhibiting the highest normal and shear strengths of $\tilde{S}_n = \tilde{s}_n^M = 381$ MPa and $\tilde{S}_s = \tilde{s}_s^M = 330.6$ MPa, respectively. With even a small volume fraction of the inclusion phase, the failure initiates along the interface between the two phases and fracture strengths reduce to values in the neighborhood of interface strengths $\tilde{s}_n^i = \tilde{s}_s^i = 287$ MPa. This corresponds to the drop of $\tilde{S}_n$ and $\tilde{S}_s$ for $v_f \to 0^+$ in comparison to those for $v_f = 0$ in fig. 16a and fig. 16b. Given the higher difference between $\tilde{s}_n^M$ and $\tilde{s}_n^i$ relative to $\tilde{s}_s^M - \tilde{s}_s^i$, we observe a sharper drop for $\tilde{S}_n$ in fig. 16a at $v_f \approx 0$ compared to that for $\tilde{S}_s$ in fig. 16b.

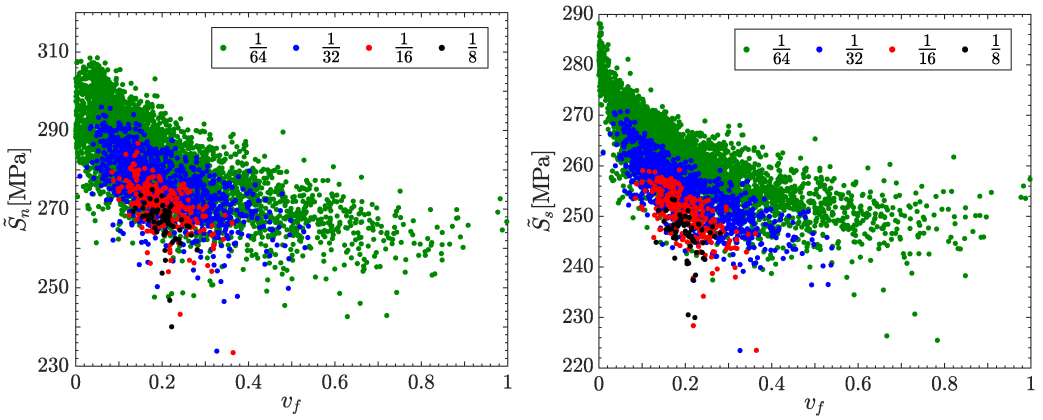

(a) Normal strength $\tilde{S}_n$ (b) Shear strength $\tilde{S}_s$

Figure 16: The variation of normal and shear strengths as a function of volume fraction for the mixed BC.

Fracture properties are expected to be very sensitive to the geometric distribution of inclusions in an SVE. As shown in fig. 16, even for the same v_f there is a significant scatter in sampled fracture strengths. This feature can be observed for all volume ratios in fig. 16 and can be contrasted to the very weak influence of the distribution of the inclusion phase on the bulk modulus in fig. 12. This contrast can be explained by the fact that the fracture response is dictated by local stress concentration points, while elastic properties average out the overall response of SVE. There are two other observations regarding the scatter in fracture strengths. First, even for the same v_f, there is a lower scatter and overall smaller fracture strengths for larger SVEs. Second, across all volume ratios the lowest fracture strengths are obtained for the intermediate range of $v_f \in [0.15, 0.8]$. This is due to the

higher likelihood of fracture initiation along interfaces between the matrix and interface phases, *cf.* §4.3.2, and the increased density of such interfaces at this intermediate range of v_f.

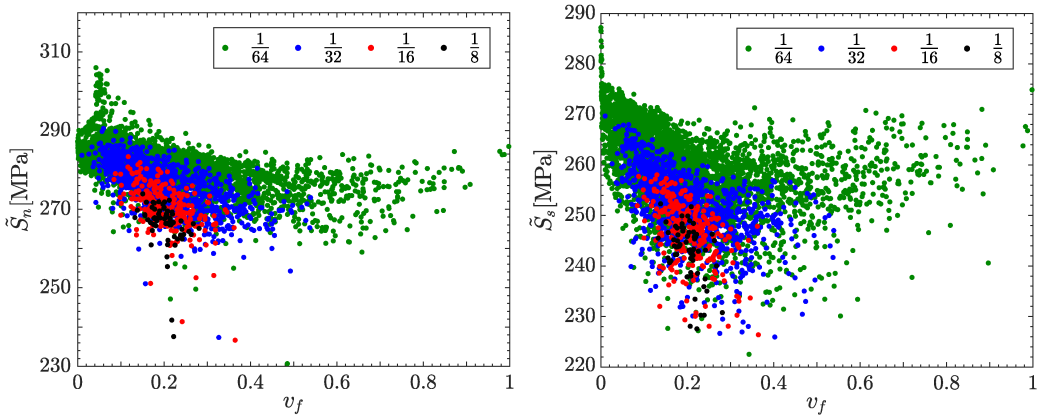

(a) Normal strength $\tilde{S}_n$ (b) shear strength $\tilde{S}_s$

Figure 17: The variation of normal and shear strengths as a function of volume fraction for the traction BC.

Except for a few minor differences, the results for traction BC, shown in fig. 17, follow the same trend discussed for mixed BC. Variations of fracture strengths, hence the standard deviation, appears to be higher for the latter. In addition, the drop in the strength near $v_f = 0$ is more severe for traction BC. This is believed to be due to lower stress concentrations around an SVE boundary at this range of v_f for mixes BC, resulting in a smoother drop of strengths from their limiting values at $v_f = 0$.

4.3.4. Distribution of fracture strengths

In this section, we study the distribution of fracture strengths for different SVE sizes. Figures 18 and 19 show PDFs of fracture strengths for mixed and traction BCs. As discussed in §4.3.3, the appearance of the secondary peaks, around $\tilde{s}_n^M = 381$ MPa and $\tilde{s}_s^M = 330.6$ MPa, in the PDFs for $l = \frac{1}{64}$ is a result of having $\approx 1.5\%$ (60 out of 4096) of SVEs in this group comprised of only the matrix phase. Similar to fig. 10 the mode of PDFs and the range of values decrease as the SVE size increases.

The size effect plots for $\tilde{S}_n$ and $\tilde{S}_s$, shown in (20), better demonstrate the effect of SVE size on these fracture strengths. Similar to fig. 11, the variation of homogenized values decrease when l increases. Clearly, this response is

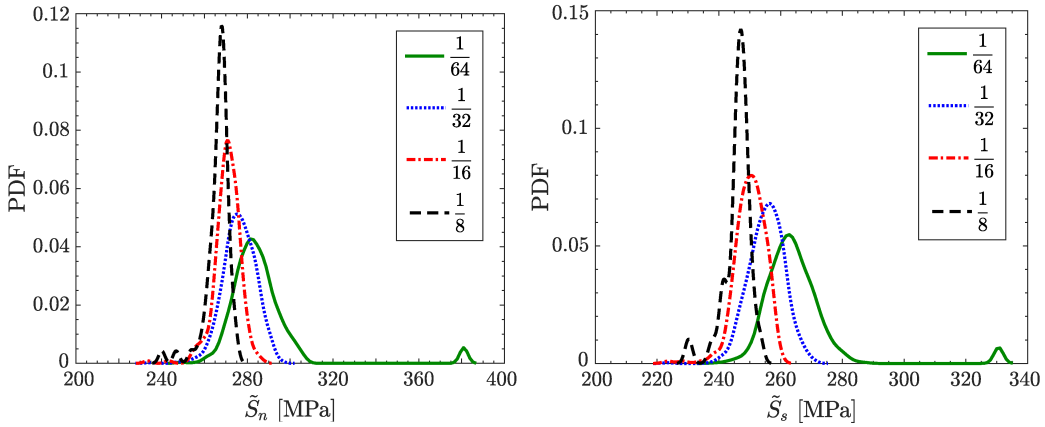

(a) Normal strength $\tilde{S}_n$ (b) Shear strength $\tilde{S}_s$

Figure 18: PDFs of normal and shear fracture strengths for different SVE sizes and the mixed BC.

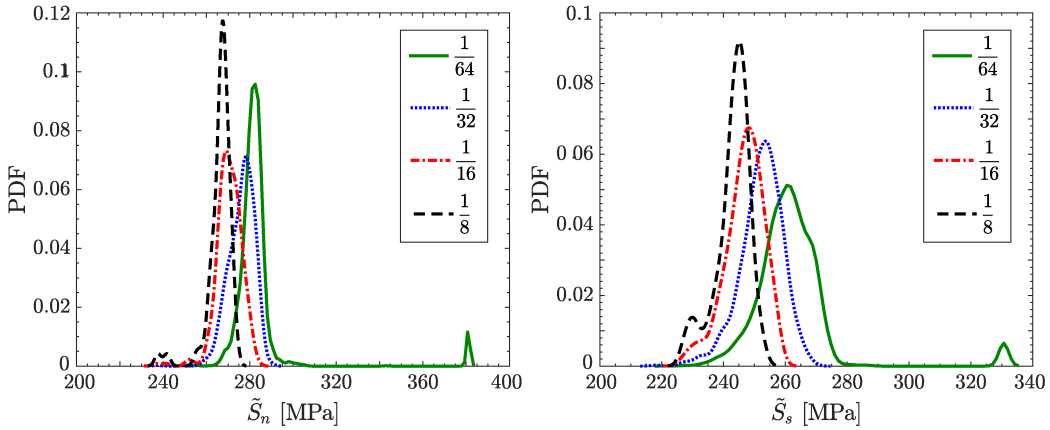

(a) Normal strength $\tilde{S}_n$. (b) Shear strength $\tilde{S}_s$.

Figure 19: PDFs of normal and shear fracture strengths for different SVE sizes and the traction BC.

expected for any homogenized property. A more interesting observation is about the variation of the mean fracture strengths. Larger SVEs in average contain a larger number of inclusions. Due to the higher population of inclusions (hence stress concentration points), SVEs are more likely to have worse stress concentration points (compared to smaller SVEs). This explains the decline of means of $\tilde{S}_n$ and $\tilde{S}_s$ as l increases. In contrast, the mean of elastic

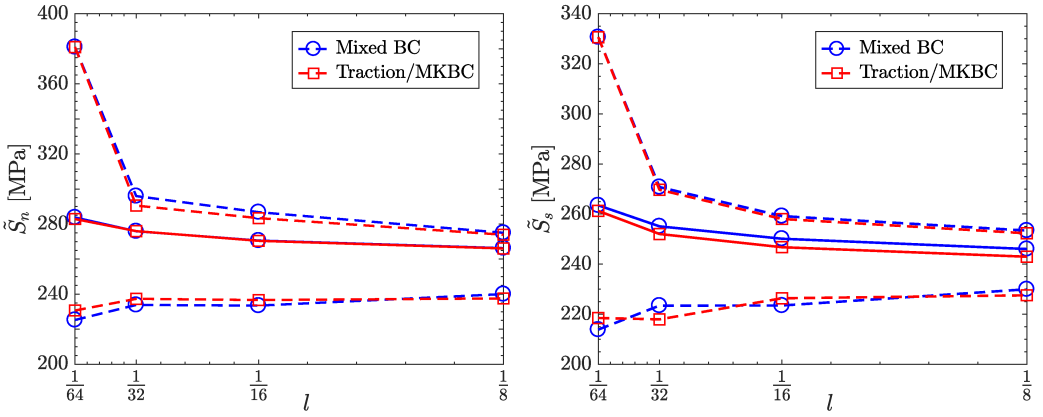

(a) Normal strength $\tilde{S}_n$ (b) Shear strength $\tilde{S}_s$

Figure 20: Minimum, maximum, and mean values of fracture strengths versus SVE size l.

properties often converge to a unique value; for this particular problem, due to the closeness of elastic moduli, the mean of κ appears to be converged from the largest sampled SVE sizes in fig. 11.

4.4. Homogenization-based fracture analysis

The goal of this section is to demonstrate the importance of material inhomogeneity in dynamic brittle fracture, a concept introduced in §2.3. Two main advantages of SVEs over phenomenological statistical models for inducing such inhomogeneity are: First, SVE-homogenized fields are microstructure-informed. Second, in phenomenological models, fracture strengths are often randomly sampled at FE nodes or quadrature points; *e.g., cf.* the Weibull sampling in [53, 12]. Therefore, the spatial correlation of the underlying field is lost through this *white noise* sampling process. In contrast, fracture strengths at the macroscopic material grid points are directly averaged from neighboring SVE-homogenized values, *cf.* §2.3 and the third subfigure in fig. 1; this naturally builds a correlation length scale, related to the morphology of the microstructure and the SVE size [3], into the macroscopic SVE-homogenized field. The second advantage is important as [82, 3] demonstrate the great impact of this correlation length on macroscopic fracture response.

While any size of SVE can be used to construct the inhomogeneous material fields for the 800 μm $\times$ 800 μm RVE, we employ the 64×64 finest grid of

$l_{\text{SVE}} = 12.5$ μm SVEs as its corresponding fields provide the closest approximation of the actual microstructure and its corresponding correlation length. Moreover, it has been shown in [3] that if relatively large SVEs are used for homogenization, the inhomogeneity is lost to an extent that certain features of brittle fracture, such as microcracking, are not captured in fragmentation simulations.

The analysis of fracture properties demonstrate their weak anisotropy, justifying the use of conservative strengths $\tilde{S}_n$ and $\tilde{S}_s$ rather than the angle-dependent strengths $\tilde{s}_n(\theta)$ and $\tilde{s}_s(\theta)$; *cf.* §4.3.1. The use of SVE-homogenized values is similar to the approach in [83], with the difference that herein instead of elastic properties, the fracture strength is treated as the inhomogeneous field. Various measures of elastic anisotropy, *cf. e.g.,* [84], range less than 3% for the homogenized stiffness tensors. This justifies the use of the elastic modulus and Poisson's ratio to characterize the homogenized isotropic material. For this material, the mean value of the elastic modulus is 502 GPa, which is very close to that obtained by linear interpolation of elastic moduli of the matrix and inclusion phases using the volume ratio of 0.2; *cf.* the results in §4.2. Aside from the aforementioned statistical aspects, fracture strength is the most important field to be considered inhomogeneous for the problems considered herein; *cf.* the discussion in §2.3.

4.4.1. Fracture under tensile loading

Figure 21 shows the results for a simple tensile loading on the 800 μm $\times$ 800 μm domain. Roller boundary condition is used on all the four edges of the domain, meaning that the normal displacement and shear traction are specified. These values are all zero except the normal velocity of the right edge which ramps up from zero to its terminal value of $\bar{v} = 5.4$ m/s in $\bar{t} = 35$ ns. The boundary conditions correspond to a 1D tensile loading on the domain in the horizontal direction for a homogeneous and isotropic material. However, right after the nucleation of the first crack, and specifically due to the inhomogeneity of the fracture strength the response of the problem is genuinely two dimensional.

Parameters of the loading on the right boundary are chosen to demonstrate the effect of the inhomogeneous field for $\tilde{S}_n$ on dynamic fracture patterns. The longitudinal wave speed is $c_{\text{d}} = 9.80$ km/s, meaning that it takes $t_W = 81.7$ ns for the wave to traverse the domain width. Thus, the ratio $\bar{t}/t_W = 0.429$ means that the wave travels about half of the domain width until it reaches its terminal value. This corresponds to a moderately fast

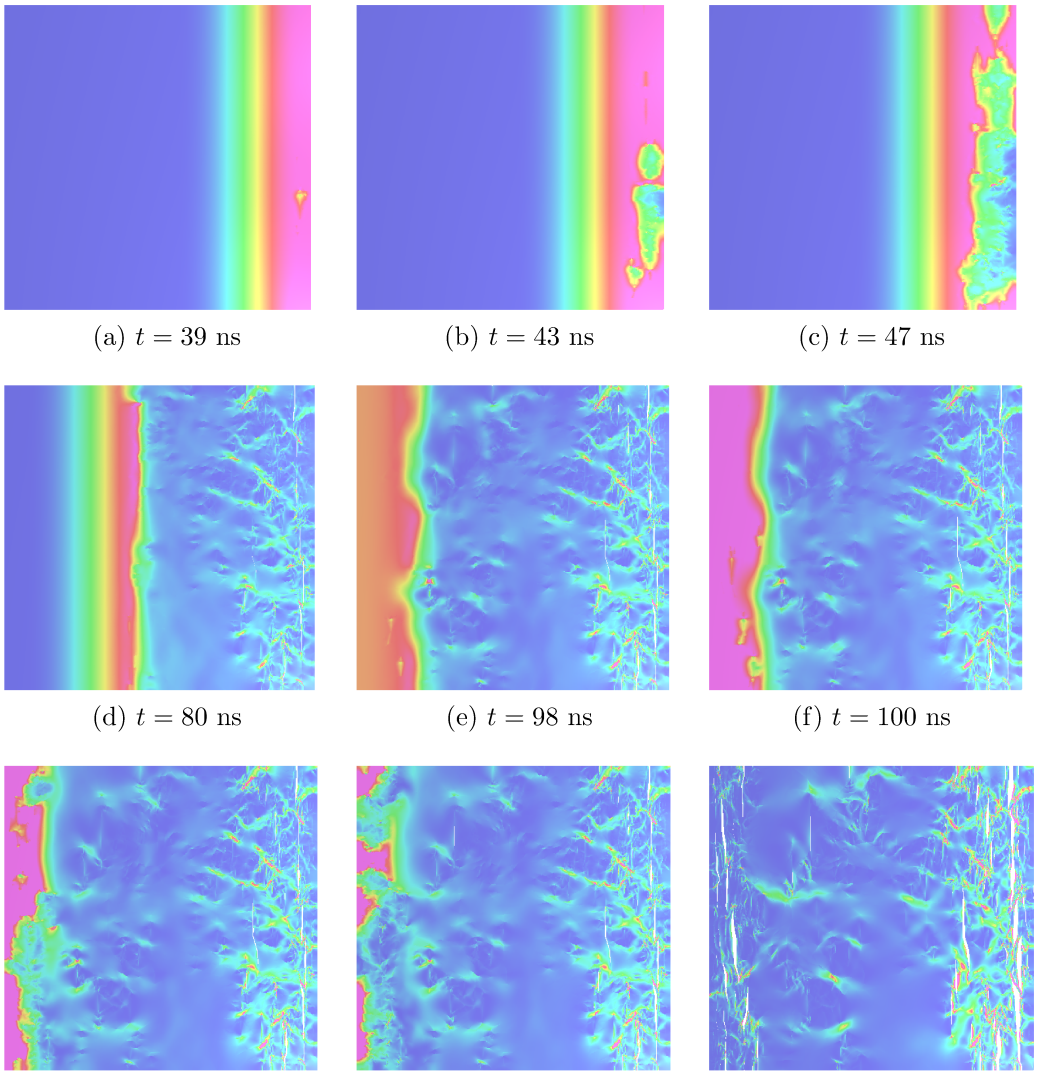

(a) $t = 39$ ns (b) $t = 43$ ns (c) $t = 47$ ns

(d) $t = 80$ ns (e) $t = 98$ ns (f) $t = 100$ ns

(g) $t = 105$ ns (h) $t = 107$ ns (i) $t = 215$ ns

Figure 21: Solution visualization for a uniaxial tensile loading on a domain with homogeneous elastic and inhomogeneous uniaxial tensile strength properties. The strain energy density is mapped to the color field, where blue to red colors correspond to zero to high strain energy densities.

rate of loading. The magnitude of the stress carried by the wave before being reflected on the left boundary is $\bar{\sigma} = 291$ MPa, while the mean value of $\tilde{S}_n$ across the whole domain is $\text{mean}(\tilde{S}_n) = 293$ MPa; *cf.* fig. 20a. Thus, if the fracture strength $\tilde{S}_n$ were homogeneous in the domain, no crack would have been nucleated in the first pass of the elastic wave. The first cracks would have been nucleated everywhere in the domain as the elastic wave reflected with twice the magnitude in stress ($2\bar{\sigma} = 582$ MPa $> \text{mean}(\tilde{S}_n)$) had traversed the domain from the left to the right boundary.

In fig. 21 the strain energy density is mapped to color, with blue to red colors corresponding to zero to high values. Figure 21a shows the solution at $t = 39$ ns, which is slightly after the inward propagating elastic wave has reached its terminal stress value of $\bar{\sigma} = 291$. The first crack nucleation is observed behind the wave front, slightly below the vertical central line of the plate. In fig. 21b this crack has further propagated and two new cracks have propagated behind the wave front. In fig. 21c, shortly after the nucleation of the first crack, the region behind the wave front is highly cracked and stress waves are significantly relaxed. Due to this relaxation and reduced transmittance of wave through the damaged zone, the amplitude of left-propagating elastic wave subdues. The lower density of crack nucleations in the middle region of the plate in fig. 21d is a direct consequence of the formation of this initial damaged zone.

The first reflection of the wave is observed in fig. 21e to fig. 21h, where upon reflection the normal stress magnitude would have doubled for an intact elastic material. The evolving high strain energy density region close to the left boundary reflects this doubling effect of the stress wave. Similar to the initial stage, where the wave entered the domain, the increased wave magnitude leaves a highly damaged region behind. Further, as shown in fig. 21g and fig. 21h, the stress relaxation shields the regions inside the domain as the reflected wave farther propagates inward.

For a fully homogeneous material the response would have been completely different; first there would have been no cracks nucleated in the first pass of the elastic wave from the right to the left boundary. Second, upon the reflection of the wave the entire height of the domain behind the doubled wave would have failed simultaneously. The response predicted by the inhomogeneous material model is clearly more realistic as cracks nucleate from the weaker sites of the material and through stress relaxation shield the neighboring areas from new crack nucleations.

The final stage of crack propagation is illustrated in fig. 21i. As observed,

cracks further propagate and open during this stage. Interestingly, for a far field velocity loading, the stress field increases upon each reflection of the waves for a fully elastic solution. However, herein due to the creation and propagation of cracks the stress fields are relaxed. In short, this example demonstrates that the inhomogeneities in the fracture field result in realistic fracture patterns even for problems that lack macroscopic stress concentration points.

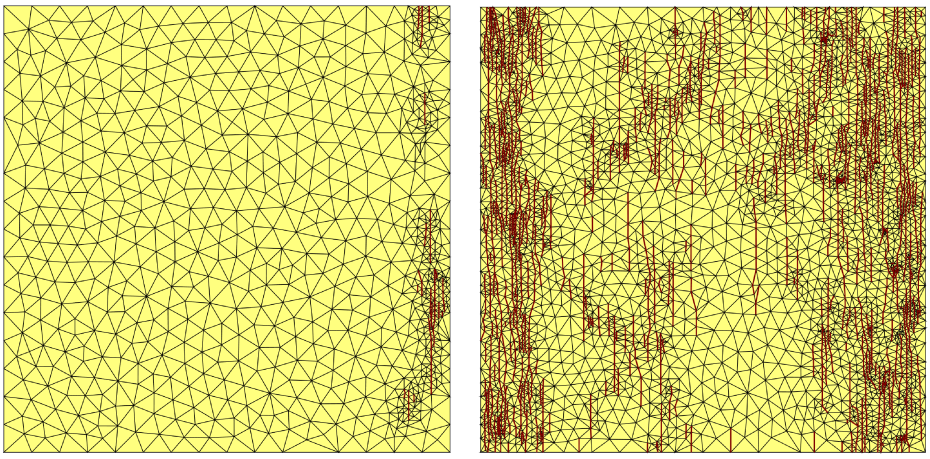

(a) $t \approx 37$ ns (b) $t \approx 215$ ns

Figure 22: Comparison of the meshes for early and final stages of the crack propagation. Crack segments on element boundaries are shown by red lines.

To demonstrate the level of mesh adaptivity that results from controlling the bulk and fracture interface errors, and from aligning element boundaries with proposed crack directions, front meshes of two stages of the solution are shown in fig. 22. Due to the asynchronicity of the aSDG method, temporal coordinate of vertices of the front are not uniform; hence reported times are approximate values for the entire spatial domain. The front meshes closely correspond to stages of the solution shown in fig. 21a and fig. 21i, respectively. We observe that the front mesh is considerably refined between these two stages. Moreover, the lower density of cracks inside the domain in fig. 22b is a result of the shielding effect of left and right damaged zones, as explained above.

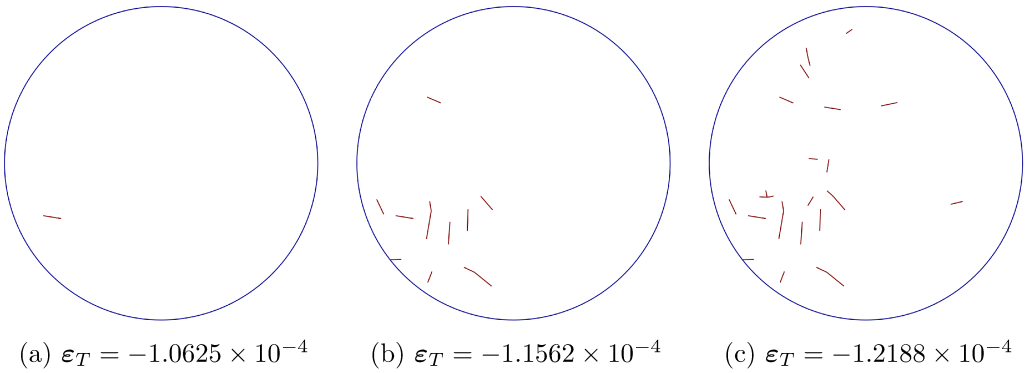

(a) $\varepsilon_T = -1.0625 \times 10^{-4}$ (b) $\varepsilon_T = -1.1562 \times 10^{-4}$ (c) $\varepsilon_T = -1.2188 \times 10^{-4}$

(d) $\varepsilon_T = -1.3125 \times 10^{-4}$ (e) $\varepsilon_T = -1.4062 \times 10^{-4}$ (f) $\varepsilon_T = -1.4375 \times 10^{-4}$

Figure 23: Crack nucleation and propagation for a circular region with fixed boundaries undergoing increasing thermal strain $\boldsymbol{\varepsilon}_T$.

4.4.2. Fracture under thermal loading

For this problem, a circular cut of radius 400 μm centered at the centroid of the 800 μm $\times$ 800 μm domain is considered. The entire circumference of the circle is fixed and the temperature is gradually decreased, resulting in a temporally increasing and spatially uniform compressive eigenstrain. Given that the thermal loading is fully specified, no heat conduction equation is solved. A circular domain is chosen to completely eliminate possible stress concentrations or anisotropy that could have resulted from the shape of the domain, *i.e.,* induced from corners of a rectangular domain. Similar to the problem in §4.4.1, $\tilde{S}_n$ is inhomogeneous. Thus, even under this spatially uniform and temporally increasing stress field, failure initiates at a location with the minimum sampled $\tilde{S}_n$, rather than predicting the nonphysical response of having the entire spatial domain failing at once. A sequence of

crack nucleation and propagation for this problem is shown in fig. 23. Figure 23a illustrates the nucleation of the first crack on the lower left side of the domain. More cracks are nucleated and propagated in figs. 23b to 23d, before much higher density of cracks are observed in the last two figures.

5. Conclusion

A packing-optimization reconstruction algorithm was employed to virtually reconstruct the distribution of inclusions in a 800 μm $\times$ 800 μm domain of a ZrB_2-SiC composite. This domain was divided to thousands of SVEs with relative edge sizes of $\frac{1}{64}$, $\frac{1}{32}$, $\frac{1}{16}$, and $\frac{1}{8}$. A non-iterative mesh generation algorithm named CISAMR was then employed to create high-quality conforming FE meshes needed to evaluate homogenized elastic properties and angle-dependent initiation tensile and shear fracture strengths of SVEs under three different boundary conditions: mixed BC, traction BC, and MKBC.

The statistical analysis of SVEs revealed interesting results. For the elastic response it was shown that the main factor affecting the homogenized bulk modulus κ was the microscopic volume ratio of inclusions, v_f. In fact, effects of the SVE size and particular arrangement of inclusions were much lower than that of v_f, such that a functional relation could be observed between v_f and κ. For SVEs with the relative size $\frac{1}{16}$, v_f varied from zero to almost unity, whereas for the largest size this range shrunk to $[0.13,\ 0.28]$. This change of the range of v_f explains the size effect observed for κ, in that its variations decreases as the SVE size increases. Furthermore, the rather linear relation between v_f and κ and the mean value of 0.2 for v_f of all sampled SVE sizes resulted in an approximately constant mean value for κ for any SVE size.

Various size effects were observed for fracture strength fields. First, as the size of SVEs increased, homogenized fracture strength fields became more isotropic. Second, unlike κ that exhibited a rather constant mean value across all SVE sizes, the mean of fracture strengths decreased for larger SVE sizes. Third, similar to κ, the variation of strengths decreased as the SVE size increased. The second and third observations are commonly known as the size effect in quasi-brittle fracture. A high dependency of fracture strengths on the particular lay-out of inclusions within an SVE was observed and unlike κ there was no clear relation between v_f and fracture strengths. In fact, the lowest fracture strengths were obtained for the intermediate ranges of v_f, which correspond to largest interface densities in SVEs. The analysis of

fracture zones support this observation in that, except for a very small percentage of smallest SVEs that did not include any inclusions, tensile failure entirely occurred at the interfaces, rather than inside the matrix or inclusion phases. The further proximity of bulk shear and interface strengths resulted in a significantly higher percentage of failures in the matrix phase under the shear loading of SVEs.

Finally, the original 800 μm $\times$ 800 μm domain was used for macroscopic dynamic fracture simulations. The inhomogeneous $\tilde{S}_n$ field obtained by the homogenization of SVEs was used as the tensile fracture strength in the context of a macroscopic interfacial damage model. Various spacetime mesh adaptive operations of the aSDG method enabled accurate resolution of fracture process zones and exact tracking of crack paths. The incorporation of material inhomogeneity was critical for the tensile stress and thermal strain problems considered, as they lack macroscopic stress concentration points. In fact, a completely different time-line and pattern of fracture would be predicted if a homogeneous fracture strength field were used. It should be noted that the statistics of the SVEs can also be used to directly realize random fields consistent with the homogenized properties; see for example [3]. Thus, by eliminating the need to homogenize new SVEs, larger computational domains can be more efficiently modeled. Moreover, the simulation of many of such realizations enables the propagation of randomness from microscale to macroscopic measures such as dissipated energy.

Many works demonstrate that by incorporating some level of material inhomogeneity, certain macroscopic characteristics of dynamic brittle fracture can accurately be captured. The approach used in this work, which is based on the analysis of SVEs, promises to be more realistic than studies relying on phenomenological statistical models for this purpose. Yet, the accuracy of the macroscopic models should be further studied. Some important extensions are: Calibrating a macroscopic fracture model beyond the linear fracture initiation limit; understanding if and how the results obtained by SVE-homogenized properties converge to those from direct numerical simulation of the microstructure; designing finite element error indicators and adaptive schemes that maintain or enhance such convergence properties. Given that the main focus of this work was on deriving SVE-homogenized properties, rather than macroscopic fracture analysis, we will investigate these questions in future research.

Acknowledgement

Abedi, Bahmani, and Clarke acknowledge partial support for this work via the U.S. National Science Foundation (NSF), CMMI - Mechanics of Materials and Structures (MoMS) program Grant No. 1538332 and and NSF CCF - Scalable Parallelism in the Extreme (SPX) program grant number 1725555. Soghrati, Yang, and Nagarajan acknowledge the funding from Air Force Office of Scientific Research (AFOSR) under Grant No. FA9550-17-1-0350, as well as partial support from the Ohio State University Simulation Innovation and Modeling Center (SIMCenter) and the allocation of computing time from the Ohio Supercomputer Center (OSC).

References

[1] A. Rinaldi, D. Krajcinovic, and S. Mastilovic. Statistical damage mechanics and extreme value theory. *International Journal of Damage Mechanics*, 16(1):57–76, 2007.

[2] M. Genet, G. Couegnat, A.P. Tomsia, and R.O. Ritchie. Scaling strength distributions in quasi-brittle materials from micro- to macro-scales: A computational approach to modeling nature-inspired structural ceramics. *Journal of the Mechanics and Physics of Solids*, 68(1):93–106, 2014.

[3] P.L. Clarke, R. Abedi, B. Bahmani, K.A. Acton, and S.C. Baxter. Effect of the spatial inhomogeneity of fracture strength on fracture pattern for quasi-brittle materials. In *Proceedings of ASME 2017 International Mechanical Engineering Congress & Exposition IMECE 2017*, page V009T12A045, Tampa, Florida, USA, 2017. IMECE2017-71515.

[4] A. Al-Ostaz and I. Jasiuk. Crack initiation and propagation in materials with randomly distributed holes. *Engineering Fracture Mechanics*, 58(5-6):395–420, 1997.

[5] J Kozicki and J Tejchman. Effect of aggregate structure on fracture process in concrete using 2D lattice model. *Archives of Mechanics*, 59(4-5):365–84, 2007.

[6] X. Yin, W. Chen, A. To, C. McVeigh, and W.K. Liu. Statistical volume element method for predicting microstructure-constitutive property relations. *Computer Methods in Applied Mechanics and Engineering*, 197(43-44):3516–3529, 2008.

[7] Zdenek P Bazant and Jaime Planas. *Fracture and size effect in concrete and other quasibrittle materials*, volume 16. CRC press, 1997.

[8] Karel Matouš, Marc GD Geers, Varvara G Kouznetsova, and Andrew Gillman. A review of predictive nonlinear theories for multiscale modeling of heterogeneous materials. *Journal of Computational Physics*, 330:192–220, 2017.

[9] W. Weibull. A statistical theory of the strength of materials. *R. Swed. Inst. Eng. Res.*, page Res. 151, 1939.

[10] W. Weibull. A statistical distribution function of wide applicability. *Journal of Applied Mechanics*, 18:293–297, 1951.

[11] R. Abedi, R.B. Haber, and A. Elbanna. Mixed-mode dynamic crack propagation in rocks with contact-separation mode transitions. In *Proceeding: 51th US Rock Mechanics/Geomechanics Symposium*, San Francisco, California, USA, 2017. ARMA 17-0679.

[12] Reza Abedi, Robert B. Haber, and Philip L. Clarke. Effect of random defects on dynamic fracture in quasi-brittle materials. *International Journal of Fracture*, 208(1-2):241–268, 2017.

[13] M. Ostoja-Starzewski. Microstructural randomness versus representative volume element in thermomechanics. *Journal of Applied Mechanics-Transactions of the ASME*, 69(1):25–35, 2002.

[14] T Kanit, S Forest, Ia Galliet, Va Mounoury, and D Jeulin. Determination of the size of the representative volume element for random composites: statistical and numerical approach. *International Journal of solids and structures*, 40(13):3647–79, 2003.

[15] W.K. Liu, L. Siad, R. Tian, S. Lee, D. Lee, X. Yin, W. Chen, S. Chan, G.B. Olson, L.E. Lindgen, M.F. Horstemeyer, Y.S. Chang, J.B. Choi, and Y.J. Kim. Complexity science of multiscale materials via stochastic computations. *International Journal for Numerical Methods in Engineering*, 80(6-7):932–978, 2009.

[16] P. Ponte Castaneda and P. Suquet. Nonlinear composites. *Advances in Applied Mechanics*, 34, 1987.

[17] P. Suquet. Continuum micromechanics. *CISM Courses and Lectures*, 272, 1997.

[18] Siavouche Nemat-Nasser and Muneo Hori. *Micromechanics: overall properties of heterogeneous materials*, volume 37. Elsevier, 2013.

[19] D. Jeulin and M. Ostoja-Starzewski. Mechanics of random and multiscale microstructures. *CISM Courses and Lectures*, 430, 2001.

[20] Martin Ostoja-Starzewski. Material spatial randomness: From statistical to representative volume element. *Probabilistic Engineering Mechanics*, 21(2):112 – 132, 2006.

[21] Matthew Mosby and Karel Matouš. Computational homogenization at extreme scales. *Extreme Mechanics Letters*, 6:68–74, 2016.

[22] S. Sakata, F. Ashida, and M. Zako. Kriging-based approximate stochastic homogenization analysis for composite materials. *Computer Methods in Applied Mechanics and Engineering*, 197(21-24):1953–1964, 2008.

[23] M. Kaminski and M. Kleiber. Numerical homogenization of n-component composites including stochastic interface defects. *International Journal for Numerical Methods in Engineering*, 47(5):1001–1027, 2000.

[24] S. Sakata, F. Ashida, and K. Enya. A microscopic failure probability analysis of a unidirectional fiber reinforced composite material via a multiscale stochastic stress analysis for a microscopic random variation of an elastic property. *Computational Materials Science*, 62:35–46, 2012.

[25] S. Sakata, F. Ashida, and K. Ohsumimoto. Stochastic homogenization analysis of a porous material with the perturbation method considering a microscopic geometrical random variation. *International Journal of Mechanical Sciences*, 77:145–154, 2013.

[26] L. Huyse and M.A. Maes. Random field modeling of elastic properties using homogenization. *Journal of Engineering Mechanics*, 127(1):27–36, 2001.

[27] J. Segurado and J. LLorca. Computational micromechanics of composites: The effect of particle spatial distribution. *Mechanics of Materials*, 38(8-10):873–883, 2006.

[28] N. Tregger, D. Corr, L. Graham-Brady, and S. Shah. Modeling the effect of mesoscale randomness on concrete fracture. *Probabilistic Engineering Mechanics*, 21(3):217–225, 2006.

[29] S.C. Baxter and L.L. Graham. Characterization of random composites using moving-window technique. *Journal of Engineering Mechanics*, 126(4):389–397, 2000.

[30] Lee M. Taylor, Er-Ping Chen, and Joel S. Kuszmaul. Microcrack-induced damage accumulation in brittle rock under dynamic loading. *Computer Methods in Applied Mechanics and Engineering*, 55(3):301 – 320, 1986.

[31] F. Homand-Etienne, D. Hoxha, and J.F. Shao. A continuum damage constitutive law for brittle rocks. *Computers and Geotechnics*, 22(2):135–151, 1998.

[32] J.F. Shao and J.W. Rudnicki. A microcrack-based continuous damage model for brittle geomaterials. *Mechanics of Materials*, 32(10):607–619, 2000.

[33] Vinh Phu Nguyen, Martijn Stroeven, and Lambertus Johannes Sluys. Multiscale continuous and discontinuous modeling of heterogeneous materials: a review on recent developments. *Journal of Multiscale Modelling*, 3(04):229–270, 2011.

[34] Y.L. Lu, D. Elsworth, and L.G. Wang. Microcrack-based coupled damage and flow modeling of fracturing evolution in permeable brittle rocks. *Computers and Geotechnics*, 49:226–44, 2013.

[35] Ming Yang, Anand Nagarajan, Bowen Liang, and Soheil Soghrati. New algorithms for virtual reconstruction of heterogeneous microstructures. *Computer Methods in Applied Mechanics and Engineering*, 338:275–298, 2018.

[36] Ming Yang, Mingshi Ji, Ehsan Taghipour, and Soheil Soghrati. Cross-linked fiberglass packs: Microstructure reconstruction and finite element analysis of the micromechanical behavior. *Computers and Structures*, 209:182 – 196, 2018.

[37] Soheil Soghrati, Anand Nagarajan, and Bowen Liang. Conforming to interface structured adaptive mesh refinement: New technique for the automated modeling of materials with complex microstructures. *Finite Elements in Analysis and Design*, 125:24 – 40, 2017.

[38] Soghrati S, Xiao F, and Nagarajan A. A conforming to interface structured adaptive mesh refinement technique for modeling fracture problems. *Computational Mechanics*, 59(4):667–684, 2017.

[39] A. Nagarajan and S. Soghrati. Conforming to interface structured adaptive mesh refinement: 3D algorithm and implementation. *Computational Mechanics*, pages 1–26, 2018.

[40] P.L. Clarke and R. Abedi. Fracture modeling of rocks based on random field generation and simulation of inhomogeneous domains. In *Proceeding: 51th US Rock Mechanics/Geomechanics Symposium*, San Francisco, California, USA, 2017. ARMA 17-0643.

[41] K.A. Acton, S.C. Baxter, B. Bahmani, P.L. Clarke, and R. Abedi. Mesoscale models characterizing material property fields used as a basis for predicting fracture patterns in quasi-brittle materials. In *Proceedings of ASME 2017 International Mechanical Engineering Congress & Exposition IMECE 2017*, pages V009T12A061, 6 pages, Tampa, Florida, USA, November 3-9, 2017. IMECE2017-71500.

[42] Katherine A. Acton, Sarah C. Baxter, Bahador Bahmani, Philip L. Clarke, and Reza Abedi. Voronoi tessellation based statistical volume element characterization for use in fracture modeling. *Computer Methods in Applied Mechanics and Engineering*, 336:135–155, 2018.

[43] Hai-Jun ZHOU, Qian FENG, Yan-Mei KAN, Le GAO, and Shao-Ming DONG. Zrb2-sic coatings prepared by vapor and liquid silicon infiltration methods: Microstructure and oxidation resistance property. , 28(10), 2013.

[44] L. Piegl and W. Tiller. *The NURBS book*. Springer Science & Business Media, 2012.

[45] D. E. Goldberg. *The Design of Innovation: Lessons from and for Competent Genetic Algorithms*. Kluwer Academic Publishers, Massachusetts, 2002.

[46] K. Deb, S. Agrawal, A. Pratap, and T. Meyarivan. A fast and elitist multi-objective genetic algorithm: NSGA-II. *IEEE Transaction on Evolutionary Computation*, 6(2):181–197, 2002.

[47] V. Tvergaard and J. W. Hutchinson. The relation between crack growth resistance and fracture process parameters in elastic-plastic solids. *Journal of the Mechanics and Physics of Solids*, 40:1377–1397, 1992.

[48] X. P. Xu and Needleman. Numerical simulations of fast crack growth in brittle solids. *Journal of the Mechanics and Physics of Solids*, 42:1397–1434, 1994.

[49] G. T. Camacho and M. Ortiz. Computational modelling of impact damage in brittle materials. *International Journal of Solids and Structures*, 33:2899–2938, 1996.

[50] Reza Abedi and Robert B. Haber. Riemann solutions and spacetime discontinuous Galerkin method for linear elastodynamic contact. *Computer Methods in Applied Mechanics and Engineering*, 270:150–77, 2014.

[51] O. Allix and A. Corigliano. Modeling and simulation of crack propagation in mixed modes interlaminar fracture. *International Journal of Fracture*, 77:111–140, 1996.

[52] A Corigliano and M Ricci. Rate-dependent interface models: formulation and numerical applications. *International Journal of Solids and Structures*, 38:547–576, 1999.

[53] N.P. Daphalapurkar, K.T. Ramesh, L. Graham-Brady, and J.F. Molinari. Predicting variability in the dynamic failure strength of brittle materials considering pre-existing flaws. *Journal of the Mechanics and Physics of Solids*, 59(2):297–319, 2011.

[54] J. Carmeliet and H. Hens. Probabilistic nonlocal damage model for continua with random field properties. *Journal of Engineering Mechanics*, 120(10):2013–2027, 1994.

[55] F. Zhou and J.F. Molinari. Stochastic fracture of ceramics under dynamic tensile loading. *International Journal of Solids and Structures*, 41(22-23):6573–6596, 2004.

[56] J. Schicker and M. Pfuff. Statistical modelling of fracture in quasi-brittle materials. *Advanced Engineering Materials*, 8(5):406–410, 2006.

[57] S. Levy and J.F. Molinari. Dynamic fragmentation of ceramics, signature of defects and scaling of fragment sizes. *Journal of the Mechanics and Physics of Solids*, 58(1):12–26, 2010.

[58] R. Abedi and R.B. Haber. Spacetime dimensional analysis and self-similar solutions of linear elastodynamics and cohesive dynamic fracture. *International Journal of Solids and Structures*, 48(13):2076–87, 2011.

[59] Belytschko T and Black T. Elastic crack growth in finite elements with minimal remeshing. *International Journal for Numerical Methods in Engineering*, 45(5):601–620, 1999.

[60] Moës N, Dolbow J, and Belytschko T. A finite element method for crack growth without remeshing. *International Journal for Numerical Methods in Engineering*, 46(1):131–150, 1999.

[61] Duarte CA, Babuška I, and Oden TJ. Generalized finite element methods for three-dimensional structural mechanics. *Computers and Structures*, 77(2):215–232, 2000.

[62] T. Strouboulis, I. Babuška, and K. Copps. The design and analysis of the generalized finite element method. *Computer Methods in Applied Mechanics and Engineering*, 181:43–69, 2000.

[63] Alejandro M Aragón and Angelo Simone. The discontinuity-enriched finite element method. *International Journal for Numerical Methods in Engineering*, 112(11):1589–613, 2017.

[64] Omid Omidi, Reza Abedi, and Saeid Enayatpour. An adaptive meshing approach to capture hydraulic fracturing. In *The 49th US Rock Mechanics/Geomechanics Symposium*, San Francisco, California, USA, 2015. ARMA 15-572.

[65] Reza Abedi, Robert B. Haber, and Boris Petracovici. A spacetime discontinuous Galerkin method for elastodynamics with element-level balance of linear momentum. *Computer Methods in Applied Mechanics and Engineering*, 195:3247–73, 2006.

[66] Reza Abedi, Morgan A. Hawker, Robert B. Haber, and Karel Matouš. An adaptive spacetime discontinuous Galerkin method for cohesive models of elastodynamic fracture. *International Journal for Numerical Methods in Engineering*, 1:1–42, 2009.

[67] R. Abedi, R. B. Haber, S. Thite, and J. Erickson. An h–adaptive spacetime–discontinuous Galerkin method for linearized elastodynamics. *European Journal of Computational Mechanics*, 15(6):619–42, 2006.

[68] Hill R. On the micro-to-macro transition in constitutive analyses of elastoplastic response at finite strain. In *Mathematical Proceedings of the Cambridge Philosophical Society*, volume 98, pages 579–590. Cambridge Univ Press, 1985.

[69] Hossein Ahmadian, Ming Yang, Anand Nagarajan, and Soheil Soghrati. Effects of shape and misalignment of fibers on the failure response of carbon fiber reinforced polymers. *Computational Mechanics*, 2018.

[70] Kenjiro Terada, Muneo Hori, Takashi Kyoya, and Noboru Kikuchi. Simulation of the multi-scale convergence in computational homogenization approaches. *International Journal of Solids and Structures*, 37(16):2285–2311, 2000.

[71] Helen M Inglis, Philippe H Geubelle, and Karel Matouš. Boundary condition effects on multiscale analysis of damage localization. *Philosophical Magazine*, 88(16):2373–2397, 2008.

[72] Sinisa Dj Mesarovic and Jagan Padbidri. Minimal kinematic boundary conditions for simulations of disordered microstructures. *Philosophical Magazine*, 85(1):65–78, 2005.

[73] Vinh Phu Nguyen, Oriol Lloberas-Valls, Martijn Stroeven, and Lambertus Johannes Sluys. Homogenization-based multiscale crack modelling: From micro-diffusive damage to macro-cracks. *Computer Methods in Applied Mechanics and Engineering*, 200(9):1220–36, 2011.

[74] Evert Hoek and Edwin T Brown. *Underground excavations in rock*. CRC Press, 1980.

[75] Eric W Neuman, Gregory E Hilmas, and William G Fahrenholtz. Strength of zirconium diboride to 2300 c. *Journal of the American Ceramic Society*, 96(1):47–50, 2013.

[76] DE Wiley, WR Manning, and O Hunter Jr. Elastic properties of polycrystalline tib2, zrb2 and hfb2 from room temperature to 1300 k. *Journal of the Less Common Metals*, 18(2):149–157, 1969.

[77] Govindaraajan B Yadhukulakrishnan, Sriharsha Karumuri, Arif Rahman, Raman P Singh, A Kaan Kalkan, and Sandip P Harimkar. Spark plasma sintering of graphene reinforced zirconium diboride ultra-high temperature ceramic composites. *Ceramics International*, 39(6):6637–6646, 2013.

[78] Munro R G. Material properties of a sintered a-sic. *J. Phys. Chem. Ref. Data*, 26(5), 1997.

[79] Bahador Bahmani, Ming Yang, Anand Nagarajan, Philip L. Clarke, Soheil Soghrati, and Reza Abedi. An integrated approach for statistical microscale homogenization to macroscopic dynamic fracture analysis. In *Proceedings of ASME 2018 International Mechanical Engineering Congress & Exposition IMECE 2018*, Pittsburgh, Pennsylvania, USA, 2018. Accepted.

[80] G. Matheron. *Estimating and Choosing. An Essay on Probability on Practice*. Springer, Berlin, 1989.

[81] Ch Lantuejoul. Ergodicity and integral range. *Journal of Microscopy*, 161(3):387–403, 1991.

[82] L.S. Dimas, T. Giesa, and M.J. Buehler. Coupled continuum and discrete analysis of random heterogeneous materials: Elasticity and fracture. *Journal of the Mechanics and Physics of Solids*, 63(1):481–490, 2014.

[83] Arash Noshadravan and Roger Ghanem. A probabilistic mesoscale damage detection in polycrystals using a random matrix approach. *Journal of Intelligent Material Systems and Structures*, 24(8):1007–17, 2013.

[84] Shivakumar I Ranganathan and Martin Ostoja-Starzewski. Universal elastic anisotropy index. *Physical Review Letters*, 101(5):055504, 2008.